Journal of Technological Operations

15th ANNIVERSARY ECORFAN Special Edition

ECORFAN-Taiwan

Journal of Technological Operations

Definition of Journal

Scientific Objectives

Support the international scientific community in its written production Science, Technology and Innovation in the Field of Engineering and Technology, in Subdisciplines production systems, mechanical properties, data transmission, process standardization, industrial engineering, composite materials, kinematic analysis, kinetic study, power generator, industrial and technological processes..

ECORFAN-Mexico SC is a Scientific and Technological Company in contribution to the Human Resource training focused on the continuity in the critical analysis of International Research and is attached to CONACYT-RENIECYT number 1702902, its commitment is to disseminate research and contributions of the International Scientific Community, academic institutions, agencies and entities of the public and private sectors and contribute to the linking of researchers who carry out scientific activities, technological developments and training of specialized human resources with governments, companies and social organizations.

Encourage the interlocution of the International Scientific Community with other Study Centers in Mexico and abroad and promote a wide incorporation of academics, specialists and researchers to the publication in Science Structures of Autonomous Universities - State Public Universities - Federal IES - Polytechnic Universities - Technological Universities - Federal Technological Institutes - Normal Schools - Decentralized Technological Institutes - Intercultural Universities - S & T Councils - CONACYT Research Centers.

Scope, Coverage and Audience

Journal of Technological Operations is a Research Journal edited by ECORFAN-Mexico S.C in its Holding with repository in Taiwan, is a scientific publication arbitrated and indexed with semester periods. It supports a wide range of contents that are evaluated by academic peers by the Double-Blind method, around subjects related to the theory and practice of production systems, mechanical properties, data transmission, process standardization, industrial engineering, composite materials, kinematic analysis, kinetic study, power generator, industrial and technological processes with diverse approaches and perspectives, That contribute to the diffusion of the development of Science Technology and Innovation that allow the arguments related to the decision making and influence in the formulation of international policies in the Field of Engineering and Technology. The editorial horizon of ECORFAN-Mexico® extends beyond the academy and integrates other segments of research and analysis outside the scope, as long as they meet the requirements of rigorous argumentative and scientific, as well as addressing issues of general and current interest of the International Scientific Society.

Arbitration Committee

Assignment of Rights

The sending of an Article to Journal of Technological Operations emanates the commitment of the author not to submit it simultaneously to the consideration of other series publications for it must complement the Originality Format for its Article.

The authors sign the Authorization Format for their Article to be disseminated by means that ECORFAN-Mexico, S.C. In its Holding Taiwan considers pertinent for disclosure and diffusion of its Article its Rights of Work.

Declaration of Authorship

Indicate the Name of Author and Coauthors at most in the participation of the Article and indicate in extensive the Institutional Affiliation indicating the Department.

Identify the Name of Author and Coauthors at most with the CVU Scholarship Number-PNPC or SNI-CONACYT- Indicating the Researcher Level and their Google Scholar Profile to verify their Citation Level and H index.

Identify the Name of Author and Coauthors at most in the Science and Technology Profiles widely accepted by the International Scientific Community ORC ID - Researcher ID Thomson - arXiv Author ID - PubMed Author ID - Open ID respectively.

Indicate the contact for correspondence to the Author (Mail and Telephone) and indicate the Researcher who contributes as the first Author of the Article.

Plagiarism Detection

All Articles will be tested by plagiarism software PLAGSCAN if a plagiarism level is detected Positive will not be sent to arbitration and will be rescinded of the reception of the Article notifying the Authors responsible, claiming that academic plagiarism is criminalized in the Penal Code.

Arbitration Process

All Articles will be evaluated by academic peers by the Double Blind method, the Arbitration Approval is a requirement for the Editorial Board to make a final decision that will be final in all cases. MARVID® is a derivative brand of ECORFAN® specialized in providing the expert evaluators all of them with Doctorate degree and distinction of International Researchers in the respective Councils of Science and Technology the counterpart of CONACYT for the chapters of America-Europe-Asia- Africa and Oceania. The identification of the authorship should only appear on a first removable page, in order to ensure that the Arbitration process is anonymous and covers the following stages: Identification of the Research Journal with its author occupation rate - Identification of Authors and Coauthors - Detection of plagiarism PLAGSCAN - Review of Formats of Authorization and Originality-Allocation to the Editorial Board-Allocation of the pair of Expert Arbitrators-Notification of Arbitration -Declaration of observations to the Author-Verification of Article Modified for Editing-Publication.

Instructions for Scientific, Technological and Innovation Publication

Knowledge Area

The works must be unpublished and refer to topics of production systems, mechanical properties, data transmission, process standardization, industrial engineering, composite materials, kinematic analysis, kinetic study, power generator, industrial and technological processes and other topics related to Engineering and Technology.

Content of Presentation

In the first article we present *Change phase materials: Wax Paraffin encapsulated in SiO_2 and SiO_2-Fe_3O_4*, by Salazar-Hernández, Carmen, Salazar-Hernández, Mercedes, Villegas-Alcaraz, José Francisco and Mendoza-Miranda, Juan Manuel, with adscription in the Instituto Politécnico Nacional, UPIIG and Universidad de Guanajuato, as second article we present *Optical fiber encoder based on phase shifting interferometry*, by López-Álvarez, Yadira Fabiola, Peña-Lecona, Francisco Gerardo, Muñoz-Maciel, Jesús and Rodríguez-Franco, Martín Eduardo, with secondment at Universidad de Guadalajara, CULagos(EPM) and Universidad Tecnológica del Norte de Aguascalientes, as third article we present *Design and simulation of a suspension system for a four-wheeled HPV*, by Contreras-Chávez, Axel A., Pérez-Cruz, Melissa Y., Villagómez-Moreno, José and Manríquez-Padilla, Carlos G, from Universidad Autónoma de Querétaro, as fourth article we present *Theoretical comparison of two shell-and-tube heat exchangers by applying different correlations*, by Huerta-Gamez, Hector, Hortelano-Capetillo, J. Gregorio, Zuñiga-Cerroblanco, J. Luis and Aguilar-Moreno, A. Alberto with assignment at the Universidad Politécnica de Juventino Rosas as last article we present *Grid-interconnected photovoltaic system as an alternative to achieve climate neutrality through the energy transition*, by Marroquín de Jesús Ángel, Castillo-Martínez, Luz Carmen, Soto-Álvarez, Sandra and Olivares-Ramírez, Juan Manuel with assignment at the Universidad Politécnica de Juventino Rosas.

Content

Article   Page

Change phase materials: Wax Paraffin encapsulated in SiO_2 and SiO_2-Fe_3O_4

Materiales de cambio de fase: Parafina encapsulada en SiO_2 y SiO_2-Fe_3O_4

Salazar-Hernández, Carmen[a], Salazar-Hernández, Mercedes[b], Villegas-Alcaraz, José Francisco[c] and Mendoza-Miranda, Juan Manuel*[d]

[a] ROR Instituto Politécnico Nacional, UPIIG • D-4418-2019 • 0000-0002-6901-2937

[b] ROR Universidad de Guanajuato, Departamento de Ingeniería en Minas, Metalurgia y Geología • LTF-1226-2024, 0000-0001-8039-8124 • 446271

[c] ROR Instituto Politécnico Nacional. ESIME-Culhuacán • ADK-2213-2022 • 0000-0002-6353-6094 • 289065

[d] ROR Instituto Politécnico Nacional, UPIIG • LTF-7054-2024 • 0000-0003-4777-767X • 295057

Abstract

Energy storage has become an essential aspect of modern energy processes, with a particular focus on enhancing the performance of thermal devices such as lithium batteries, which are widely regarded as a key technology in the transition to electric vehicles. In instances where the placement of heat removal systems is necessary to prevent the device from heating up, this paper study the storage capacity of a bioorganic phase-change material (PCM) encapsulated in silica nanoparticles. This PCM is obtained from sodium silicate (MS) and its modification with magnetite (MS-Fe_3O_4). The PCM was integrated into the silica matrix through impregnation, and infrared spectroscopy demonstrated the presence of its primary functional groups. Furthermore, thermal characterization curves were obtained, indicating a significant impact on the temperature holding time when the PCM was absorbed into the silica matrix modified with magnetite.
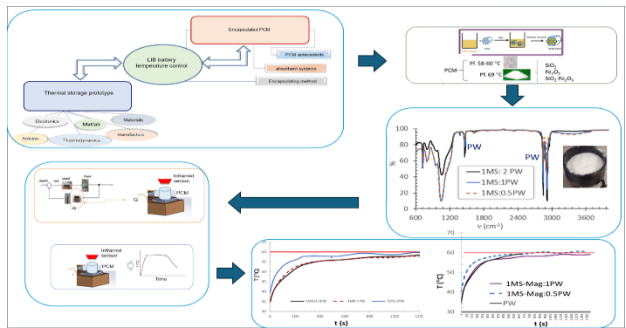
Resumen

El almacenamiento de energía es vital para mejorar diferentes procesos energéticos entre los cuales se encuentran la mejora de dispositivos térmicos como son las pilas de litio empleadas en los autos eléctricos. Donde se requiere colocar sistemas removedores de calor para evitar el calentamiento del dispositivo, es por ello que en este proyecto se propone estudiar la capacidad de almacenamiento de un PCM bio-orgánico encapsulado en nanopartículas de sílice, obtenidas a partir de silicato de sodio (MS) y su modificación con magnetita (MS–Fe_3O_4). El PCM se integró a la sílice por impregnación y la espectroscopia de infrarrojo indicó la presencia de los principales grupos funcionales de éste; por otra parte, se obtuvieron las curvas de caracterización térmica observando un efecto en el tiempo de sostenimiento de temperatura cuando se absorbe el PCM en la sílice modificada con la magnetita.

PCM; SiO_2; SiO_2/Fe_3O_4; energy

PCM; SiO_2; SiO_2/Fe_3O_4; energy

RENIECYT
Registro Nacional de Instituciones y Empresas Científicas y Tecnológicas

1702902 CONAHCYT

Introduction

Lithium batteries have transformed numerous industries, including consumer electronics and electric vehicles, due to their high energy density and rechargeability. However, they are subject to several challenges, with temperature rise being one of the most significant. When a lithium battery is overheated, it may experience several adverse effects that compromise its performance and safety. One of the most serious consequences is the accelerated deterioration of internal components, including electrolytes and electrodes. This can result in a reduction in storage capacity and an overall decrease in battery lifespan, Oró (2012), Villasmil (2019), Mohammadian (2017), Rao (2011), Jeon (2011).

As illustrated in Figure 1, the lithium-ion battery (LIB) is constructed according to the configuration of an electrochemical cell, comprising a cathode and anode separated to prevent a short circuit. The cathode (positive charge) is composed of lithium oxide (Li_2O) and varying quantities of transition metals (specifically, nickel, Ni; magnesium, Mg; and cobalt, Co). In contrast, the anode (negative charge) is formed of graphite. The transfer of electrons occurs from the anode to the cathode.

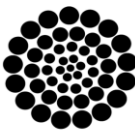The anode is connected to the cathode via an electrolyte medium, which facilitates the transfer of charge carriers, namely Li^+ ions, dissolved in an aprotic medium, such as diethyl carbonate or conductive polymers, including polyvinylidene fluoride (PVDF) and polyvinyl fluoride (PVP).

Box 1
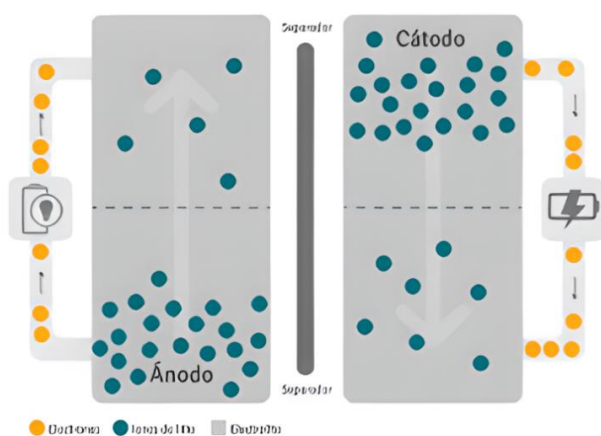
Figure 1

Operation of a lithium-ion battery (LIB)

The flow of electrons from the anode to the cathode is responsible for producing the battery voltage. The movement of Li^+ ions through the electrodes maintains equilibrium between the external current and the system, ensuring that the positive charge of the Li^+ ions does not neutralize the external charge (Mohammadian 2017).

One of the limitations of this energy storage system is the generation of heat during the charging and discharging cycle of the LIB, which, if not adequately managed, can cause damage to some components within a relatively short time frame. Furthermore, if the temperature rises to the point of melting the lithium (180°C), the metal will be subject to an exothermic reaction and will explode. Such temperatures can be reached in high-voltage storage systems. This requires the implementation of temperature regulation systems (60-85°C) (Rao 2011), such as phase change materials (PCM), which possess a high latent heat (melting or boiling) or sensible heat and are used as thermal energy storage (Jeon 2011).

Therefore, these materials have been using as prospective new energy storage systems, specifically in the context of thermal energy storage (TES). Figure 2 shows the storage principle, which involves the absorption of energy by the material, followed by its release upon a change in temperature.

This release may occur as latent or sensible heat. The storage of energy using sensible heat ($Q=Cp\Delta T$) requires that the material possess a high Cp value. The quantity of energy that can be stored is dependent upon the temperature differential (ΔT) to which the PCM is subjected.

Therefore, the temperature of both the storage and the energy release are not constant. However, storage through latent heat (phase change) occurs at the temperature at which the phase change of matter (solid-liquid; solid-gas; liquid-gas; liquid-gas) is generated, which occurs at a constant temperature or in a very limited temperature range for all materials (Jeon 2011, Hussain 2016).

Box 2
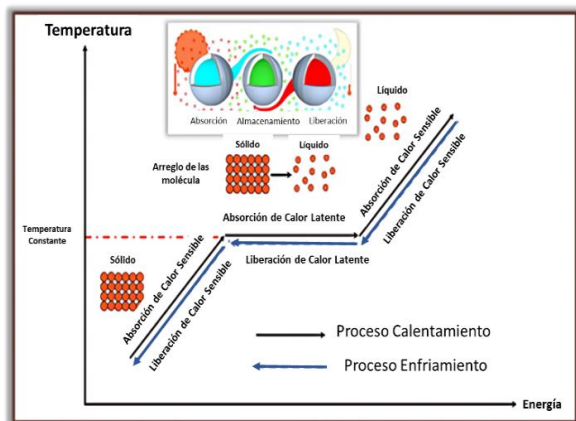
Figure 2

Operation of PCM as an energy storage device [5,6]

Consequently, the aim of this project is to investigate the potential of kerosene wax as a temperature controller for a LIB (Figure 3). The aim is to determine the ability to control the temperature of the system at 60°C. To improve the stability of the PCM, it is encapsulated in three different systems. The materials under consideration are magnetite (a thermal conductor), mesoporous silica (a thermal insulator), and silica modified with magnetite (a hybrid material).

Box 3
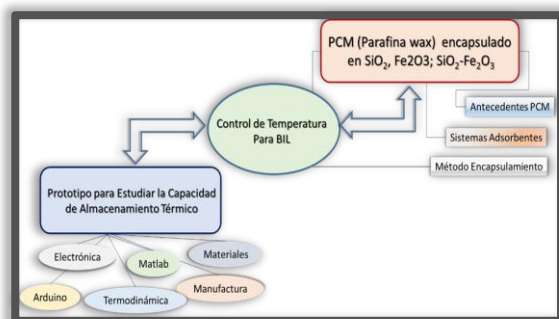
Figure 3

Plan for obtaining a temperature controller for lithium-ion batteries (LIB)

Experiments

To implement the analysis, a series of steps were undertaken to identify an appropriate material for the temperature controller function. Figure 4 shows the general methodology developed for this project. Stage 1 involved encapsulating the PCM in SiO_2, Fe_3O_4, and SiO_2/Fe_3O_4 systems. Stage 2 required adapting the equipment to obtain data. Stage 3 focused on thermal characterization of the materials, with results presented in graphical form for comparison.

Box 4
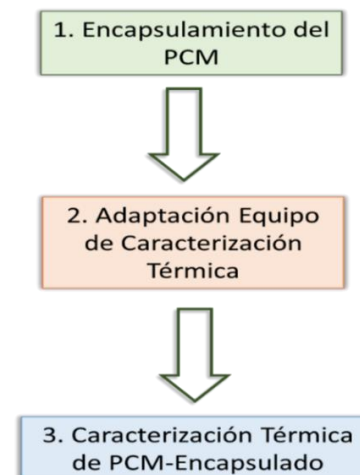
Figure 4

General project methodology

Magnetite synthesis and characterization

The synthesis of magnetite was conducted via precipitation techniques, in accordance with the conditions set forth in Equation 1, with a $2Fe^{3+}:Fe^{2+}$ ratio. In a 250-ml flask, 5.27 g of $FeSO_4$ and 2.7 g of $FeCl_3$ were dissolved in 200 ml of water under constant stirring. The pH was then adjusted to 10–11 with NH_4OH, and the system was placed at reflux for 24 hours. At the conclusion of the specified period, the magnetite was retrieved through filtration and subjected to a 12-h drying process at 75°C. The magnetite was subjected to powder XRD analysis, which was conducted on a Rigaku Ultima IV X-ray diffractometer.

$$2FeCl_3 + FeSO_4 + 8NH_4OH \rightarrow Fe_3O_4 + (NH_4)2SO_4 + 6NH_4Cl + 4H_2O \qquad (1)$$
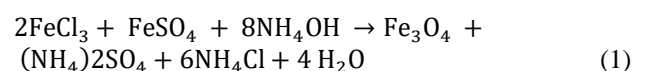
Magnetite MS synthesis and modification

The synthesis of mesoporous silica materials was conducted using sodium silicate and P–123 as a molecular sieve, according to the methodology proposed by Salazar et al. (Salazar-Hernández 2020). Silicic acid is obtained and aged for 24 h, then used as a precursor in the formation of the inorganic network. The magnetite is anchored in the silica by modifying it with amino groups. Finally, 0.167 moles of the mesoporous silica are suspended in 100 mL of ethanol. A solution of 0.0416 moles of the modifying agent 3–aminopropyltrimethoxysilane (90%, Aldrich) was prepared, and 1 mL of NH_4OH was added.

Salazar-Hernández, Carmen, Salazar-Hernández, Mercedes, Villegas-Alcaraz, José Francisco and Mendoza-Miranda, Juan Manuel. [2024]. Change phase materials: Wax Paraffin encapsulated in SiO2 and SiO2-Fe3O4. Journal of Technological Operations. 8[21]1-7: e1821107.
https://doi.org/10.35429/JTO.2024.8.21.1.8

Article

The system was then subjected to reflux for 24 h. At the conclusion of this period, the solid was recovered and washed with two portions of 10 mL of ethanol and 10 mL of acetone. It is then subjected to a 12 h drying process at 75°C in an oven. The anchoring of the magnetite in the modified silicas was conducted by placing 1 g of the synthesized Fe_3O_4 under reflux with 10 g of MS-NH_2 for 12 h. Then, the material was recovered by filtration and dried at 70°C for 12 h.

Wax paraffin encapsulation

The PCM used was wax paraffin (99%; Aldrich) with a melting point between 58 and 60 °C. The encapsulation process was conducted via impregnation (Figure 5), employing the quantities specified in Table 1. The PW was placed in a boiling flask and heated until complete melting occurred. Then, the encapsulant was added and mixed homogeneously, and the mixture was allowed to cool to room temperature.

Box 5
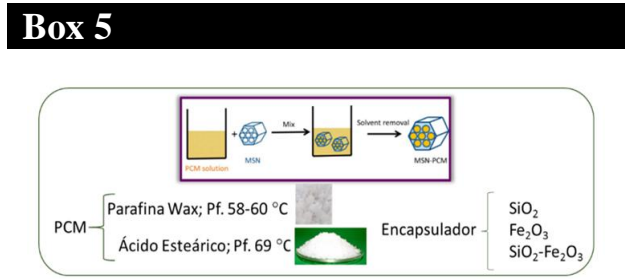
Figure 5

Impregnation method of PCM in encapsulation systems

Box 6

Table 1

Aggregate of PCM added to each encapsulator

PCM (g)	0.05	0.1	0.2
% weight	10	20	40

Thermal characterization

To obtain the data from the various samples, an experimental setup will be designed in accordance with the specifications depicted in Figure 6. This setup is intended to facilitate temperature measurements, which will be conducted on the different PCM encapsulations.

The measurements will be conducted with the use of a PID thermometer. To ensure accurate temperature control, a REX-100 thermostat will be employed as the heat source.

The thermostat will enable the regulation of the temperature supplied via a resistor connected to the thermometer. This experimental approach will provide the controlled conditions necessary for the accurate and systematic measurement of the thermal behavior of the encapsulated PCMs.

Box 7
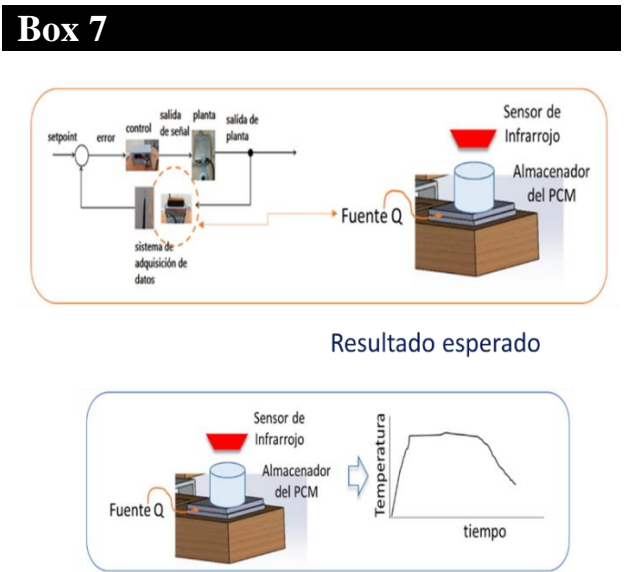
Figure 6
Apparatus for thermal characterization.

Results

PCM impregnation in encapsulators

The encapsulation method used was simple impregnation. Figure 7a shows the infrared spectra for the wax paraffin, which presents signals corresponding to a C–H hydrocarbon at 2900 cm^{-1}, ν and 1400 cm^{-1}, δ. Additionally, the spectra identify a C=C at 680 cm^{-1}. While the MS shown signals corresponding to the inorganic network, specifically Si–O–Si at 1100 and 780 cm^{-1}, as well as a shoulder at 980 cm^{-1}, which is associated with Si–OH. Magnetite is not active in the infrared, therefore, in the MS modification with magnetite, only a broadening of the Si–O–Si band (1100 cm^{-1}) is observed. Figure 7b shows the diffractogram for magnetite, in which the characteristic planes were identified. These are 2θ at 30.1, 35.4, 43.1, 54.5, 57.6, and 62°, which correspond to magnetite according to Mohammadi et al. (Mohammadi [2021]).

Salazar-Hernández, Carmen, Salazar-Hernández, Mercedes, Villegas-Alcaraz, José Francisco and Mendoza-Miranda, Juan Manuel. [2024]. Change phase materials: Wax Paraffin encapsulated in SiO2 and SiO2-Fe3O4. Journal of Technological Operations. 8[21]1-7: e1821107. https://doi.org/10.35429/JTO.2024.8.21.1.8

Journal of Technological Operations
Article

Box 8

(a)

(b)
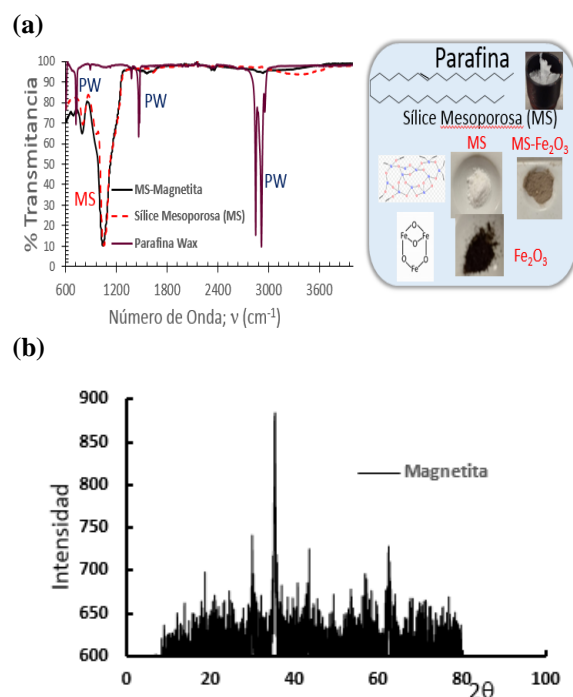
Figure 7

Base materials (a) Infrared spectra for encapsulators and PCM (b) XRD for magnetite

Figure 8a shows the magnetite modified with PCM, wherein all the corresponding signals for the hydrocarbon (PW) and a broad band of 700–1100 cm^{-1}, indicative of the interaction of Fe$_3$O$_4$ with paraffin, are observed. Furthermore, the solid formed with low (1:0.2) and high (1:2) concentrations of PCM solid pastes were obtained. In contrast, mesoporous silica (Figure 8b) forms powder-type solids at low PCM concentrations (1:0.5), granulated solids at 1:1 concentration, and pastes at 1:2 concentrations.

The intensity of the PW signals increases with increasing PW content in the material, reaching a maximum at the 1:2 concentration (Figure 8c). For MS-magnetite, the PW forms a granular solid at a concentration of 1:0.5, while a paste was observed at the other two concentrations, 1:1 and 1:2, respectively. In the spectra for the 1:0.5 concentration, the intensity of the silica and PW signals is relatively similar.

However, at a concentration of 1:1, the PW signals show a clear predominance in intensity.

Box 9

(a)

(b)

(c)
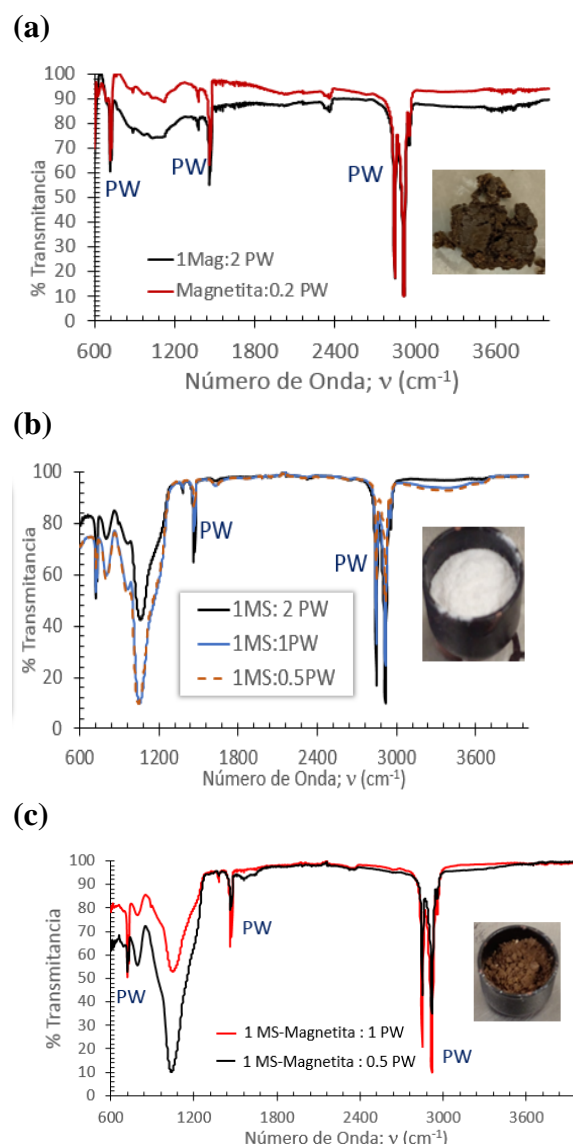
Figure 8

Encapsulation of PCM. (a) Paraffin Wax (b) Magnetite (c) Mesoporous Silica (MS)

Thermal characterization

Once the PW has been successfully melted, it forms a cover on the vessel and is unable to recover its initial volume (Figure 9a). This behavior has also been observed with magnetite as an encapsulator. However, in the case of MS and MS-magnetite, the volumes remain constant.

As shown in Figure 9b, the wax paraffin is heated to reach 60°C. This temperature was reached in 761 seconds (12.68 minutes) in the PW and in 792 seconds (13.2 minutes) in the magnetite with 20% PW (1:0.2). After this point, the temperature begins to increase, rising by 1°C. This is due to the conductive capacity of magnetite (Fe$_3$O$_4$). The 1:2 mixture exhibited a higher heat adsorption rate, reaching 60°C at 418 seconds (6.97 minutes).

Salazar-Hernández, Carmen, Salazar-Hernández, Mercedes, Villegas-Alcaraz, José Francisco and Mendoza-Miranda, Juan Manuel. [2024]. Change phase materials: Wax Paraffin encapsulated in SiO2 and SiO2-Fe3O4. Journal of Technological Operations. 8[21]1-7: e1821107.
https://doi.org/10.35429/JTO.2024.8.21.1.8

Following this, the temperature was maintained at a range of 1–2°C above 60°C, with minor fluctuations.

Box 10

(a)

Antes de Fundir   Después de Fundir

(b)
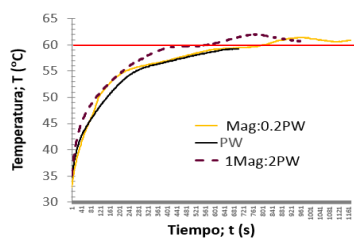
(c)
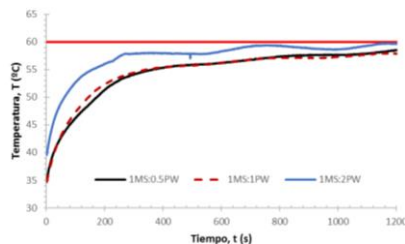
(d)
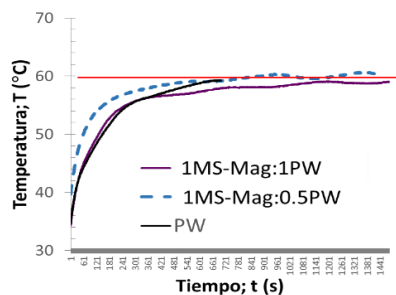
Figure 9

Thermal behavior (a) PCM volume change by the heating-cooling cycle (b) Thermal load curve of PCM encapsulated in Fe_3O_4 (c) Thermal load curve of PCM encapsulated in MS (d) Thermal load curve of PCM encapsulated in MS-Fe_3O_4.

Mesoporous silica behaves as a thermal insulator (characterized by low thermal conductivity), preventing the temperature from reaching 60°C. Consequently, at a ratio of 1:0.5 (Figure 9c), the temperature difference was observed to be 1.39–5 °C. At a ratio of 1:1, the temperature difference was 2–5°C, while at a ratio of 1:2, the temperature difference was 1–2 °C. The behavior of silica encapsulated with magnetite exhibited a hybrid character between that of a conductor and a thermal insulator, with a ΔT of less than ±0.5°C (Figure 9d).

Conclusions

The results of the infrared spectroscopy characterization indicate that the modification of silica with magnetite enhances the adsorption of PCM on the solid surface, as evidenced by the observed hybrid behavior between the insulator (SiO_2) and conductor properties of the magnetite.

Declarations

Conflict of interest

The authors declare no interest conflict. They have no known competing financial interests or personal relationships that could have appeared to influence the article reported in this article.

Author contribution

Salazar-Hernández, Carmen: Conception and design, data collection, analysis and interpretation of the data, critical revision of the manuscript.

Salazar-Hernández, Mercedes: Conception and design, data collection, analysis and interpretation of the data, critical revision of the manuscript.

Villegas-Alcaraz, José Francisco: Data collection, analysis and interpretation of the data, critical revision of the manuscript.

Mendoza-Miranda, Juan Manuel: Conception and design, data collection, analysis and interpretation of the data, critical revision of the manuscript.

Availability of data and materials

Data will be made available on request.

Funding

Acknowledgements

Salazar-Hernández, Carmen, Salazar-Hernández, Mercedes, Villegas-Alcaraz, José Francisco and Mendoza-Miranda, Juan Manuel. [2024]. Change phase materials: Wax Paraffin encapsulated in SiO2 and SiO2-Fe3O4. Journal of Technological Operations. 8[21]1-7: e1821107.
https://doi.org/10.35429/JTO.2024.8.21.1.8

Article

Abbreviations

LIB	Lithium-Ion Battery
MS	Mesoporous Silica
PCM	Phase Change Material
PID	Proportional, Integral and Derivative controller
PVDF	Polyvinylidene fluoride
PVP	Polyviniyl fluoride
PW	Wax paraffin
XRD	X-ray Diffraction Analysis

References

Antecedents

Hussain, A., Tso, C.Y., Chao, C.Y.H. [2016] Experimental investigation of a passive thermal management system for high-powered lithium ion batteries using nickel foam-paraffin composite. Energy, 115, 209–218.

Jeon, D.H., Baek, S.M. [2011] Thermal modeling of cylindrical lithium-ion battery during discharge cycle. Energy Convers. Manage, 52, 2973–2981.

Kwon, J. H., Wilson, Lee D., Sammynaiken, R. [2014]. Synthesis and characterization of magnetite and activated carbon binary composites. Synthetic Metals,197, 8–17.

Basics

Lenders, J.J.M., Mirabello, G., Sommerdijk, N.A.J. [2016] Bioinspired magnetite synthesis via solid precursor phases. Chem. Sci. 7, 5624–5634.

Mohammadi, H.R., Nekobahr, E., Akhtari, J., Saeedi, M., Akbari, J., Fathi, F. [2021]. Synthesis and Characterization of Magnetite Nanoparticles by Co-precipitation Method Coated with Biocompatible Compounds and Evaluation of In-Vitro Cytotoxicity. Toxicology Reports. 8, 331-336.

Mohammadian, S.K., Zhang, Y [2017]. Cumulative effects of using pin fin heat sink and porous metal foam on thermal management of lithium-ion batteries. Applied Thermal Engineering, 118, 375–384

Support and differences

Oro, E. Gil, A., Miró, L., Peiró, G., Álvarez, S., Cabeza, L.F. [2012]. Thermal Energy Storage Implementation Using Phase Change Materials for Solar Cooling and Refrigeration Applications. Energy Procedia, 30, 947–956.

Rao, Z., Wang, S., Zhang, G. [2011]. Simulation and experiment of thermal energy management with phase change material for ageing LiFePO$_4$ power battery. Energy Convers. Manage, 52; 3408–3414.

Salazar-Hernández, M., Salazar-Hernández, C., Rangel-Porras, G., Corona-Arroyo, M. [2020]. Efecto del grupo funcional en la adsorción de Ag(I) en soluciones sintéticas con materiales mesoroprosos de silica. Revista de Ingeniería Industrial, 4(11): 24–30.

Villasmil, W., Fischer, L. J., Worlitschek, J. [2019]. A review and evaluation of thermal insulation materials and methods for thermal energy storage systems. Renewable and Sustainable Energy Reviews, 103, 71–84

Optical fiber encoder based on phase shifting interferometry

Encoder de fibra óptica basado en interferometría de cambio de fase

López-Álvarez, Yadira Fabiola*[a], Peña-Lecona, Francisco Gerardo[b], Muñoz-Maciel, Jesús[c] and Rodríguez-Franco, Martín Eduardo[d]

[a] ROR Universidad de Guadalajara, CULagos(EPM) and Universidad Tecnológica del Norte de Aguascalientes • T-1555-2018, • 0000-0002-9041-1908 • 375952

[b] ROR Universidad de Guadalajara, CULagos • 0000-0002-9537-8633 • 122563

[c] ROR Universidad de Guadalajara, CULagos • 0000-0001-7091-6573 • 123153

[d] ROR Universidad Tecnológica del Norte de Aguascalientes• T-1539-2018 • 0000-0002-6804-4777 • 660892
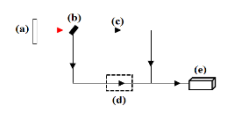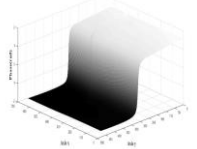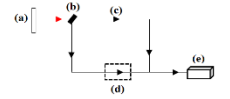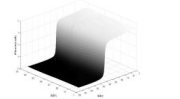
Abstract

In an automated industrial system monitoring and controlling the position of moving objects represents a crucial element in processes that have rotating systems.This is regularly in robots that use internal sensors to monitor the position of their joints. In this work we present the study of an optical encoder based on a Mach Zehnder interferometer. To determine the phase, the Phase Shift Interferometry algorithm was use, using five steps. The optical fiber encoder used the rotation matrix, and the results were correlated with those obtained by the optical technique, the reported behavior shows a wide similarity between the optical encoder and the simulated. The experimental design showed a differential distance of 0.0452 rad between the initial and that obtained after deformation. We report an encoder capable of recovering the initial phase, showing a difference in the correlation of 0.0000925 u.a.

Optical fiber encoder based on phase shifting interferometry.		
Objective Demonstrate the interferometric encoder capability. Check the sensor behavior demonstrated by simulation.	**Methods** Optical technique: Phase shifting interferometry. Use of optical fiber interferometer as transducer. **Experimental design** Mach-Zehnder interferometer	**Results** The encoder is highly robust, capable of recovering its initial phase, with a differential distance of 0.0452 rad.

Optical encoder, optical fiber, Mach Zehnder interferometer

Resumen

En un sistema industrial automatizado el monitoreo y control de la posición de objetos en movimiento representa un elemento importante en los procesos que cuentan con sistemas giratorios. Esto se presenta con regularidad en los robots que utilizan sensores internos para monitorear la posición de sus articulaciones. En este trabajo presentamos el estudio de un encoder óptico a base de un interferómetro Mach Zehnder. Los resultados se analizaron utilizando la técnica de interferometría por desplazamiento de fase de cinco pasos. El encoder de fibra óptica se simuló a través de la matriz de rotación y los resultados se correlacionaron con los obtenidos por la técnica óptica de cinco pasos, mostrando un comportamiento en la fase óptica similar. El diseño experimental mostro una distancia diferencial de 0.0452 rad entre la fase inicial y la obtenida después de la deformación, el encoder mostrado fue capaz de recuperar la fase inicial, mostrando una diferencia en la correlación de 0.0000925 u.a.

Optical fiber encoder based on phase shifting interferometry.		
Objetivo Demostrar la capacidad de encoder interferométrico. Comprobar el comportamiento del sensor mostrado mediante simulación.	**Metodología** Técnica óptica: Phase shifting interferometry. Uso de interferómetro de fibra óptica como transductor. **Diseño experimental** Interferómetro Mach-Zehnder	**Resultados** Se muestra encoder con alta robustez, es capaz de recuperar su fase inicial, con una distancia diferencial de 0.0452 rad

Encoder óptico, fibra óptica, Interferómetro Mach Zehnder

Journal of Technological Operations   8[21]1-8: e2821108
Article

Introduction

The development of systems for measuring physical variables, such as rotation, has applications in the automotive, marine and aerospace industries [1,2]. The first mechanical devices to record the angular changes of an object are reported as gyroscopes [3]; later, electromechanical devices such as the encoder emerged. However, technological advances force such devices to present greater advantages over everyday mechanical and electromechanical instruments, so the implementation and development of optical sensors has been increasingly accepted [4].
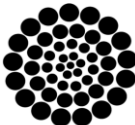
An encoder can be linear or angular, depending on the application; they base their operation on changing codes depending on the angle of rotation of the object and can provide a measurement with nanometric resolution, they are used in a wide range of control systems, manufacturing, robots, among many others [5-9]. Among the techniques for the use of optical encoders, the phase recovery of two wavefronts through cross-correlation techniques, diffraction and polarisation, these techniques have been able to recover the phase and correlate with angles of 0.031 degrees, other studies have proposed the measurement in a range of 18 degrees, even measurements have been made with 100 degrees, obtaining an accuracy of 0.2 degrees [10-16].

On the other hand, the advances in the field of interferometric encoders based on optical fibre compared to optical encoders is their high resolution, a construction focused directly on the robustness of the transducer, electromagnetic immunity, high sensitivity and its measurement is non-destructive, allowing its incorporation in systems where space is reduced, Its operating principle is based on the modulation of light by means of the length of the optical fibre and considering the output response of the sensor, monitoring the disturbance at a single point of the fibre and obtaining a correlation with the phase, amplitude, frequency and polarisation. However, to obtain an interferometric signal it is necessary to use optical arrays called interferometers, among these are Sagnac, Fabry-Perot and Mach-Zehnder, their difference lies in the ranges of measurement of the displacements caused by the induced deformation.

If, in addition to using interferometric systems, the use of fibre optics is incorporated, what would be obtained is a device that is not dependent on environmental changes and external vibrations [20-27].

Despite the advances that have been made so far, having a robotic system that works and is monitored 360 degrees can be a complicated task, due to the type of sensors that are being used, even the mechanical design itself can mean a limitation in the working range of the robot, this fact makes it necessary to add links to the robotic system, as well as specialised sensors, involving a high monetary cost.

Another problem presented in the navigation of robotic systems is their localisation, both in the uncertainty of estimating the position of a robot, as well as in the accumulated error in its movement [28 ,8], due to this, the use of an encoder capable of monitoring the complete rotation of a robotic joint functioning directly as a transducer, that can provide fast and reliable localisation of the system, that works in hostile environments, with high precision, repeatability in measurement, with a reduced size and that also helps new designs of reliable instruments, are the reasons for the study of the behaviour of a fibre optic encoder based on interferometry.

The main contribution of this work lies in showing an interferometric encoder capable of measuring full angular movements without restrictions, recovering its initial position, as well as verifying the behaviour of the sensor shown by simulation. The interferometer encoder shows high measurement stability, high repeatability, low differential distance (hysteresis) and low cost; it is conditioned according to the ranges of rotation, due to the characteristics of the rotating mechanical element. It can be used in robotic systems, as its design characteristics allow it to monitor 360 degrees of joint rotation.

Methodology

Model development

When light propagates through an optical fibre, it is required that the wave equation and Maxwell's equations are satisfied, obtaining an electromagnetic field pattern transverse to the direction of propagation [29,30].

Article

If the intensity at the output of the optical fibre is directly linked to the field distribution, it can be expressed by equation 1.

$$I_i(x,y) = A(x,y) + B(x,y)\cos(\varphi(x,y)) \quad [1]$$

Where A, B and φ, are the background intensity, intensity modulation and phase, respectively. If the intensity detected by a sensor shows disturbances, Equation 1 shall be modified in the cosine argument by the term α_f, equation 2.

$$I_f(x,y) = A(x,y) + B(x,y)\cos(\varphi(x,y) + \alpha_f) \quad [2]$$

The difference between the two intensity states I_i and I_f, the initial and final, respectively, result in a geometrical arrangement known as interference fringes, with spatial coordinates (x, y), these stripes are reciprocal to the two states of deformation, as the deformation of the object changes, so does the distribution of these stripes. The absolute value of the difference between I_i and I_f, can be written as follows:

$$|I_f - I_i| = I_M|\cos\varphi_f - \cos\varphi_i| \quad [3]$$

To monitor the system disturbances, it is necessary to perform an analysis of the geometrical distribution of the interference fringes, as well as the extraction of the phase resulting from these two deformation states.

The demodulation of these interference fringes results in the characteristic parameters of the measurement; filtering and phase unwrapping are necessary [31].

One of the most widely used techniques that shows great acceptability is *Phase shifting interferometry*, in which a series of interferograms with phase differences is recorded, as shown in equation 2. To perform the phase reconstruction process, in general, algorithms are applied with a combination of the interferograms; the analysis can be done with interferograms [32]

$$tan\varphi = \frac{\sum_{n=1}^{M} b_n I_n}{\sum_{n=1}^{M} a_n I_n} \quad [4]$$

With a_n and b_n, as real coefficients.

To obtain the pase φ, con the phase shift technique, it was considered that the optical path shift is determined by equation 5 where θ is given in intervals of $\frac{\pi}{2}$.

$$R(\hat{z},\theta) = \begin{pmatrix} \hat{x}\cos\theta - \hat{y}\sin\theta \\ \hat{x}\sin\theta + \hat{y}\cos\theta \\ \hat{z} \end{pmatrix} \quad [5]$$

Taking five interferograms with [33,34]:

$$\alpha_{f1} = \hat{x}\cos\theta - \hat{y}\sin\theta \quad [6]$$
$$\alpha_{f2} = \hat{x}\sin\theta + \hat{y}\cos\theta \quad [7]$$

Using trigonometric identities we arrive at the wrapped phase equation with five interferograms given by [35]:

$$\varphi_w = \tan^{-1}\left(\frac{2(I_3(x,y) - I_1(x,y))}{I_4(x,y) + I_0(x,y) - 2I_2(x,y)}\right) \quad [8]$$

Finally, the method for unwrapping the phase consists of modifying $\pm 2\pi$ to the pixel being unwrapped.

Development of experiments

For the development of the encoder, a Mach Zehnder interferometer based on single mode fibre optics was built, Figure 1. A Helium-Neon laser light source at 632.8 nm and a microscope objective at 20X was used.

Box 1
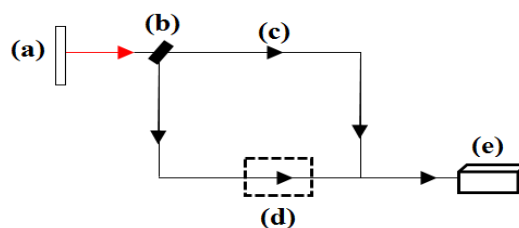
Figure 1
Mach-Zehnder interferometer for interferometric encoder (a) Source, (b) Beamsplitter, Fibre optics: (c) Reference, (d) External disturbance and (e) CCD
Own elaboration

Experimental results

A set of interferograms with a phase difference of π/2 were obtained, Figure 2 shows the interferograms obtained with the arrangement in Figure 1.

Figure 2 shows for (a) 0, (b) 90, (c) 180, (d) 270 and (c) 360 degrees of rotation in one of the interferometer arms, showing an increase in the number of fringes..

Box 2
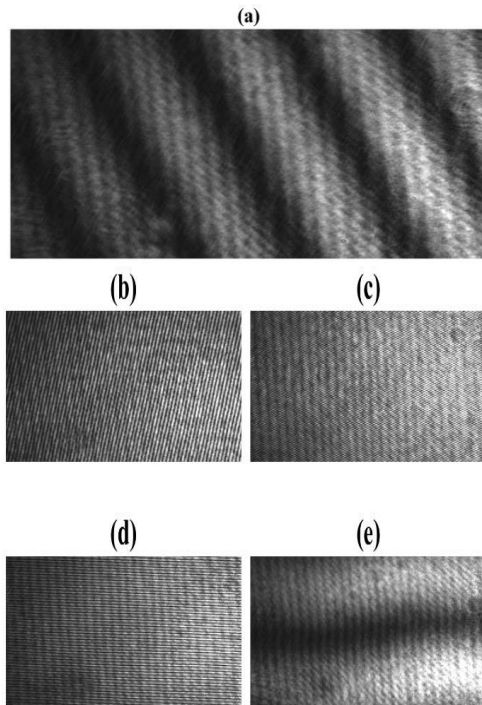
Figure 2

Encoder interference fringes using Mach-Zehnder interferometer, with θ: (a) 0, (b) 90, (c) 180, (d) 270 and (c) 360 degrees.

Box 3
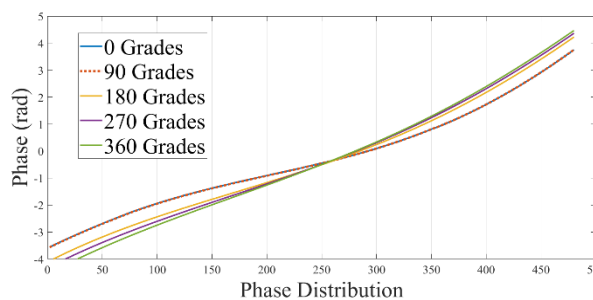
Figure 3

Encoder phases using Mach Zehnder interferometer, from 0 to 360 degrees

Own elaboration

Figure 3, shows the phase distribution resulting from the demodulation of each interferogram, the behaviour suggested by these phases is ascending, in the centre of the phase maps an intersection point is observed, to later show a descending behaviour.

Figure 4 illustrates the behaviour of the phase map unwrapped from the resulting values with , and using the algorithm represented by equation 8.

To check the robustness of the encoder, as well as its behaviour, rotation angles were chosen randomly, as indicated in equations 6 and 7, the behaviour of the unwrapped phase map is shown in Figure 5, which shows a sigmoid function, around 50% of the phase distribution.

Box 4
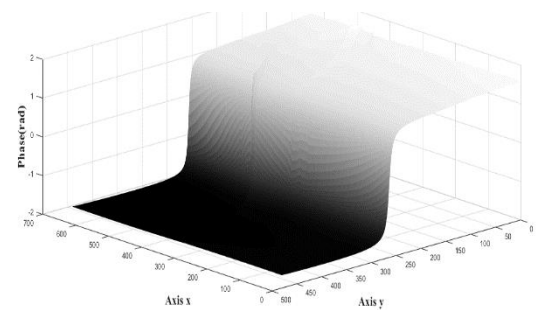
Figure 4

Experimental encoder phase map, using Mach Zehnder interferometer, I_n,n=5

Box 5
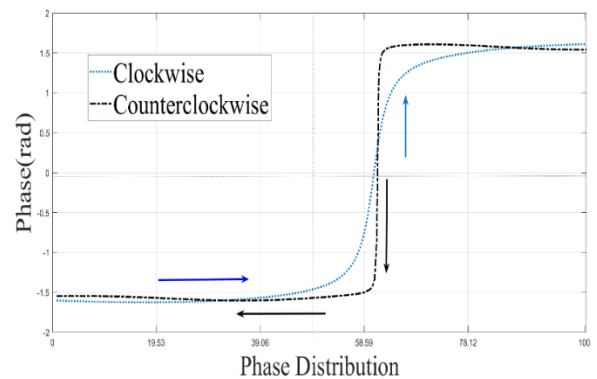
Figure 5

Title Phase map using Mach Zehnder interferometer with I_n,n=5.

To check the results the system was simulated equations 2, 6 and 7, the phase profile of the rotation is shown in Figure 6, (a) indicates the behaviour for , while (b) shows the phase behaviour for , both using five interferograms.

López-Álvarez, Yadira Fabiola, Peña-Lecona, Francisco Gerardo, Muñoz-Maciel, Jesús and Rodríguez-Franco, Martín Eduardo. [2024]. Optical fiber encoder based on phase shifting interferometry. Journal of Technological Operations. 8[21]1-8: e2821108.
https://doi.org/10.35429/JTO.2024.8.21.1.8

Box 6
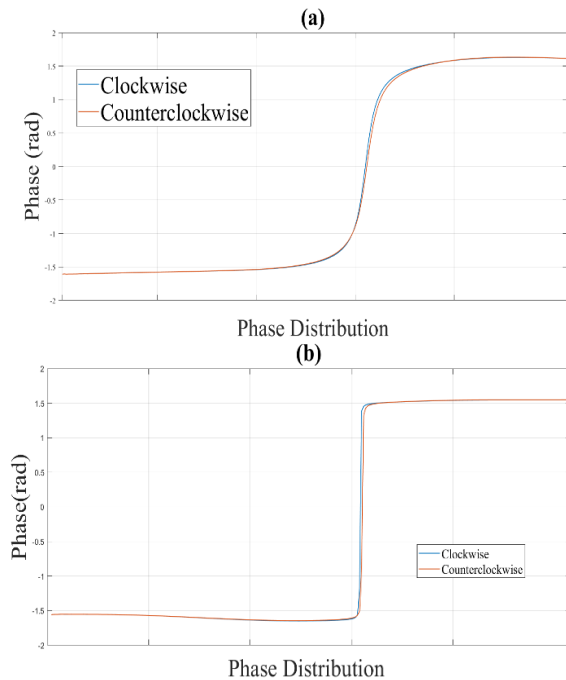
Figure 6

Phase map profile, interferometric encoder simulation with: (a) equation [6] and (b) equation [7]

To verify that the encoder is able to recover its initial position, in addition to comparing the experimental and simulated results, the differential distance of the initial phase, zero degrees, as well as the Pearson correlation coefficients were calculated for equations 5 and 6.

Figure 7 shows the behaviour of the Pearson correlation coefficients, the behaviour of the encoder shows for the case of the initial position a coefficient of 0.99990, as the fibre optic encoder is rotated the behaviour of the coefficients show an upward trend, where the maximum correlation is obtained in the phase map obtained at 320 degrees.

The sensitivity of the encoder is dependent on the rotation of the fibre.

Box
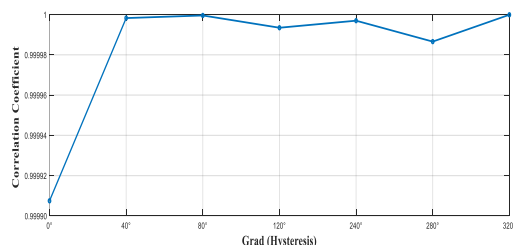
Figure 7

Correlation coefficients between turns with hysteresis
Own elaboration

Acknowledgement

Conclusions

This work shows the results obtained in the study of the behaviour of an interferometric encoder, a comparison was made between the experimental and simulated development using the concepts of rotation matrix that govern the behaviour of a rotating robotic system.

For the analysis of the phase maps the PSI technique was used, the interferometric model for the phase wrapped with .

The encoder shown, in addition to its robust design, is capable of recovering its initial phase, with a very small differential distance, where the behaviour of the correlation coefficients is dependent on the rotation.

The interferometric encoder shown is capable of being conditioned to measurements of very small degrees, as it is able to adjust to the rotating system being used. These results provide a guideline for analysing its use in the navigation and localisation of robotic systems.

Declarations

Conflict of Interest

The authors declare that they have no conflict of interest.

Authors' contribution

López-Álvarez, Yadira Fabiola: Experimentation, analysis of results and mathematical modelling.

Peña-Lecona, Francisco Gerardo: Experimental design, previous studies

Muñoz-Maciel Jesús: Demodulation of interference fringes

Rodríguez-Franco, Martín Eduardo: Research and review.

López-Álvarez, Yadira Fabiola, Peña-Lecona, Francisco Gerardo, Muñoz-Maciel, Jesús and Rodríguez-Franco, Martín Eduardo. [2024]. Optical fiber encoder based on phase shifting interferometry. Journal of Technological Operations. 8[21]1-8: e2821108.
https://doi.org/10.35429/JTO.2024.8.21.1.8

Funding

This research was carried out in the optics and photonics laboratory of the CULagos, UDG and with the support of CONAHCYT.

Acknowledgements

To the Consejo Nacional de Humanidades, Ciencia y Tecnología CONAHCYT, Initial postdoctoral stay (2023), CVU: 375952.

To the Universidad Tecnológica del Norte de Aguascalientes, UTNA, for support in the realisation of stage 1 of prototypes of optical sensors in educational robotic systems.

References

Background

[1]   Huggins, R. W., Abbas, G. L., Hong, C. S., Miller, G. E., Porter, C. R., & Van Deventer, B. (1992). Fiber-coupled position sensors for aerospace applications. Optics and Lasers in Engineering, 16(2–3), 79–103

[2]   A. R. Missie, P. L. William, L. Antonio, and D. B. Alexandre. (2017). Angular velocity estimation from incremental encoder measurements in the presence of sensor imperfections, IFAC-PapersOnLine, 50: 5979–5984

[3]   Passaro, V. M. N., Cuccovillo, A., Vaiani, L., De Carlo, M., & Campanella, C. E. (2017). Gyroscope Technology and Applications: A Review in the Industrial Perspective. Sensors, 17(10), 2284. https://doi.org/10.3390/s17102284.

[4]   Giallorenzi, T. G., Bucaro, J. A., Dandridge, A., Sigel, G. H., Cole, J. H., Rashleigh, S. C., & Priest, R. G. (1982). Optical Fiber Sensor Technology. IEEE Journal of Quantum Electronics, 18(4), 626–665,

[5]   M.V. Shishova, S.B. Odinokova, D.S. Lushnikova, A.Y. Zherdeva, O.A. Guryleva. (2017). Mathematical modeling of signal transfer process into optical system of a linear displacement encoder, Procedia Engineering 201, 623–629

[6]   R. J. Tansey and S. Holly. (1988). Development Of An Interferometric Encoder For High Resolution Angular Measurements, Proc. SPIE 0887, Acquisition, Tracking, and Pointing

[7]   Ji-hua Zhang and Lilong Cai. (1998). Autofocus laser rotary encoder, Appl. Opt. 37, 2691-2695

[8]   Haoxiang Lang, Ying Wang and C. W. de Silva. (2008). Mobile robot localization and object pose estimation using optical encoder, vision and laser sensors, IEEE International Conference on Automation and Logistics, Qingdao, pp. 617-622.

[9]   Lafolla, L., Filipozzi, M., Freund, S., Zam, A., Rauter, G., & Cattin, P. C. (2020). Proof of concept of a novel absolute rotary encoder. Sensors and Actuators, A: Physical, 312

Basics

[10]   Percival F. Almoro, Giancarlo Pedrini, Arun Anand, Wolfgang Osten, and Steen G. Hanson (2009).Angular displacement and deformation analyses using a speckle-based wavefront sensor, APPLIED OPTICS / Vol. 48, No. 5

[11]   Yamaguchi, I., & Fujita, T. (1989) Laser speckle rotary encoder. Applied Optics, 28(20), 4401

[12]   Yamaguchi, I. (1989). Encoder and strain gauge using laser speckle. Optics and Lasers in Engineering, 11(4), 223–232.

[13]   Fernando Perez Quintián, Ariel Lutenberg, and María Aurora Rebollo. (2006). Study of an incremental optical encoder using speckle, Proc. SPIE 6341, Speckle06: Speckles, From Grains to Flowers, 634121,

Support

[14]   Angelika Taubner, Hans-Jürgen von Martens. (1998). Measurement of angular accelerations, angular velocities and rotation angles by grating interferometry, Measurement 24 21–32

[15] Nathalie Mancier, Ayoub Chakari, Patrick Meyrueis, and Michel Clément. [1995] Angular displacement fiber-optic sensor: theoretical and experimental study, Vol. 34, No. 28, APPLIED OPTICS

[16] Mertz, L. N. (1991). Interferometric angle encoder. *Review of scientic instruments*, 62(5), 1356-1360.

Diferences

[17] D. Felekis and E. Papadopoulos. (2010). Design and development of a low-cost interferometric device for nanoscale position and velocity feedback, *IEEE/ASME International Conference on Advanced Intelligent Mechatronics*, Montreal, QC, Canada, pp. 611-616.

[18] P. Drabarek and R. M. Kennel Fiet. (2008), Are interferometric encoders a reasonable alternative in servo drive applications, *4th IET Conference on Power Electronics, Machines and Drives*, York, pp. 149-153.

[19] D. Gardner, T. Hofler, S. Baker, R. Yarber and S. Garrett, (1987). A fiber-optic interferometric seismometer, in *Journal of Lightwave Technology*, vol. 5, no. 7, pp. 953-960.

[20] Kurzych, A., Kowalski, J., Sakowicz, B., Krajewski, Z. & Jaroszewicz, L. (2016). The laboratory investigation of the innovative sensor for torsional effects in engineering structures monitoring. *Opto-Electronics Review*, 24(3), 134-143.

[21] Wang, L., & Fang, N. (2017). Applications of Fiber-Optic Interferometry Technology in Sensor Fields. InTech. doi: 10.5772/66276

[22] Kidwell, R., Miller, R., Bennett, S., Dyott, R., Allen, D., & Brunner, J. (1998). Fiber optic rate gyros as replacements for mechanical gyros. Guidance, Navigation, and Control Conference and Exhibit.

[23] Budinski, V., & Donlagic, D. (2019). A Miniature Fabry Perot Sensor for Twist/Rotation, Strain and Temperature Measurements Based on a Four-Core Fiber. *Sensors*, 19(7), 1574.

[24] S. -H. Hsu, C. -Y. Tsou and J. -C. Hsu. (2012). Interferometric fiber strain sensor, *2012 IEEE 3rd International Conference on Photonics*, Pulau Pinang, Malaysia, 2012, pp. 114-115,

[25] H. W. Chow, N. C. Cheung and W. Jin. (2010). A Low-Cost Submicrolinear Incremental Encoder Based on 3 ×3 Fiber-Optic Directional Coupler, in *IEEE Transactions on Instrumentation and Measurement*, vol. 59, no. 6, pp. 1624-1633,

[26] Kurzych, A. T., Jaroszewicz, L. R., Krajewski, Z., Dudek, M., & Kowalski, J. K. (2019). Interferometric optical fiber sensor set for angular velocity recording: Allan variance analysis in practice. In K. Kalli, S. O'keeffe, & G. Brambilla (Eds.), Seventh European Workshop on Optical Fibre Sensors (Vol. 11199, pp. 1–4).

[27] Elvira-Ortiz, D. A., Romero-Troncoso, R. D. J., Jaen-Cuellar, A. Y., Morales-Velazquez, L., & Osornio-Rios, R. A. (2016). Vibration suppression for improving the estimation of kinematic parameters on industrial robots. *Shock and Vibration*,(1), 6954012

Discussion

[28] Munoz-Barron, B., Rivera-Guillen, J.R., Osornio-Rios, R.A. *et al*. (2015). Sensor Fusion for Joint Kinematic Estimation in Serial Robots Using Encoder, Accelerometer and Gyroscope. *J Intell Robot Syst* **78**, 529–540.

[29] Luis Ramos, A., Martí Panameño, E., & Díaz, H. R. (2001). Cálculo de los modos electromagnéticos en una fibra óptica mediante soporte computacional analítico. *Revista Mexicana de Física*, 47(4), 386-391.

[30] Freund, I. Joseph W. Goodman. (2008). Speckle Phenomena in Optics: Theory and Applications. *J Stat Phys* **130**, 413–414.

[31] Kjell J. Gåsvik, (2002). Optical Metrology, John Wiley & Sons Ltd, 3ed, 316

[32] J. Schwider, R. Burow, K.-E. Elssner, J. Grzanna, R. Spolaczyk, and K. Merkel. (1993). Digital wave-front measuring interferometry: some systematic error sources, Appl. Opt. 22, 3421-3432

[33] Milligan, T. (1999). More applications of Euler rotation angles. IEEE Antennas and Propagation Magazine, 41(4), 78-83.

[34] Bajd, T., Mihelj, M., Munih, M. (2013). Rotation and Orientation. In: Introduction to Robotics. SpringerBriefs in Applied Sciences and Technology. Springer, Dordrecht.

[35] P. Hariharan, B. F. Oreb, and T. Eiju. (1987), Digital phase-shifting interferometry: a simple error-compensating phase calculation algorithm, Appl. Opt. 26, 2504-2506.

Design and simulation of a suspension system for a four-wheeled HPV

Diseño y simulación de un sistema de suspensión para un HPV de cuatro ruedas

Contreras-Chávez, Axel A. [a], Pérez-Cruz, Melissa Y. [b], Villagómez-Moreno, José*[c] and Manríquez-Padilla, Carlos G. [d]

[a] ROR Universidad Autónoma de Querétaro• LTF-7342-2024 • 0009-0000-7834-8873 •1345044
[b] ROR Universidad Autónoma de Querétaro • LTF-7178-2024 • 0009-0002-0515-9806 •1345042
[c] ROR Universidad Autónoma de Querétaro• LTY-7778-2024 • 0000-0001-7044-9282 •1035567
[d] ROR Universidad Autónoma de Querétaro • JKH-7361-2023 • 0000-0003-1332-5173 •347939

Abstract

This work presents the design and simulation of a suspension system for a four-wheel, single-rider human-powered vehicle (HPV) to enhance stability and maneuverability on uneven terrain. The system, designed with lightweight components such as springs and shock absorbers available on the market, avoids the use of complete commercial suspensions. Static structural analyses using finite element methods were conducted to evaluate materials and geometries, along with dynamic simulations in MSC ADAMSDD. A comparison of the vertical and lateral displacement of the center of mass between the proposed system and a similar commercial model showed a 50% reduction in vertical displacement. This system improves impact absorption and HPV stability while meeting functional requirements and using accessible materials, making it an effective and cost-efficient solution for this type of vehicle.
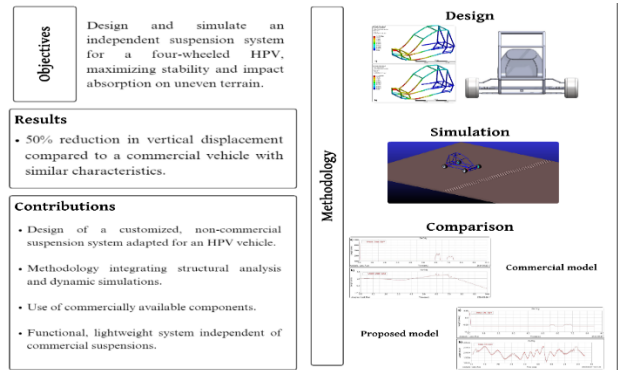
Resumen

En este trabajo se presenta el diseño y simulación de un sistema de suspensión para un vehículo de propulsión humana (HPV) de cuatro ruedas y un tripulante, que mejora la estabilidad y maniobrabilidad ante irregularidades del terreno. El sistema, diseñado con componentes ligeros como resortes y amortiguadores disponibles comercialmente, evita el uso de suspensiones completas. Se realizaron análisis estructurales estáticos con elementos finitos para evaluar materiales y geometrías, además de simulaciones dinámicas en MSC ADAMSDD. Comparando el desplazamiento vertical y lateral del centro de masa del diseño propuesto frente a un modelo comercial similar, se obtuvo una reducción del 50% en el desplazamiento vertical. Este sistema mejora la absorción de impactos y la estabilidad del HPV, cumpliendo con los requisitos funcionales y utilizando materiales accesibles, lo que lo convierte en una solución eficaz y económica para vehículos de este tipo.
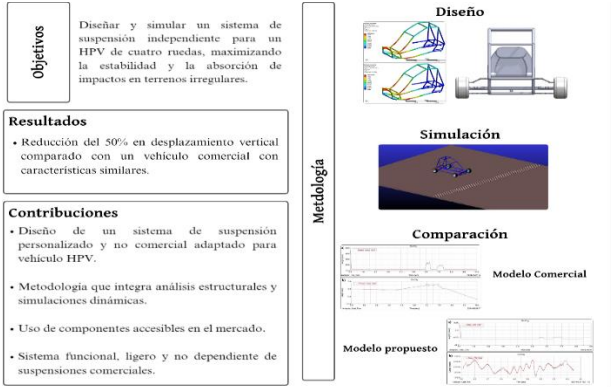
Mechanical-Design, FEA, Dynamic-Simulation

Diseño-mecánico, FEA, Simulación-dinámic

RENIECYT
Registro Nacional de Instituciones y Empresas Científicas y Tecnológicas

1702902 CONAHCYT

Journal of Technological Operations 8[21]1-8: e3821108
Article

Introduction

The suspension system is one of the most important when talking about vehicles, as it has a direct impact on passenger comfort. This system not only keeps the passenger comfortable, but also has a mechanical function, which isolates the body from the irregularities of the terrain, damping the disturbances that occur through the tyres. Explicitly, it is determined that the suspension of a vehicle is the set of organs and parts that are responsible for absorbing and damping the irregularities that occur when driving, which prevents the oscillations that originate in the wheels (due to the driving conditions) from being transmitted to the occupants of the vehicle; in such a way that the adherence of the wheels to the ground and the stability of the vehicle is favoured (Cebolla, 2017).

Suspension systems are classified according to the behaviour of their components during movement and disturbances. Dependent suspensions connect the wheels via a rigid axle, transmitting the movement from one wheel to the other. In contrast, independent suspensions (see Figure 1) allow each wheel to oscillate vertically without affecting the other, adapting better to pavement conditions (Vázquez, 2011).

Box 1
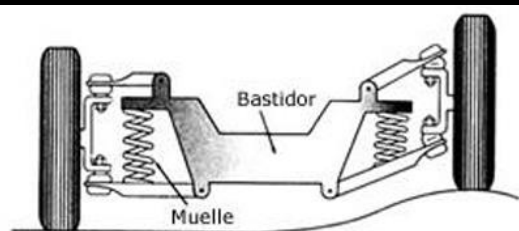
Figure 1

Independent suspension system

Source: Onion, 2017

Recent studies have focused on optimising both the structural stiffness and dynamic behaviour of vehicles, using advanced techniques such as Finite Element Analysis (FEA) and dynamic simulations. For example, Pulido (2014) performed a ¼ and ½ vibrational analysis of the Formula Student vehicle, determining the natural frequencies of the suspension to optimise shock absorption and improve the system's rebound and pitch response.

Additionally, their study on mass transfer during acceleration and braking demonstrated a significant improvement in vehicle stability, increasing the vehicle's handling under demanding conditions. In the field of lighter vehicles, such as go-karts, Gonza (2023) highlights that, although they lack a suspension system, the structural design of the chassis withstands torsional and bending stresses, providing the necessary rigidity to handle loads during acceleration and cornering, improving overall stability. Similarly, in the design of the Formula SAE electric single-seater, Auquilla & Torres (2016) performed a dynamic analysis with ADAMS/Car software, where they simulated constant radius curves and straight-line obstacles, validating the suspension design. Their results showed improvements in camber variation and spring movement, which contributed to better handling and stability, highlighting a low centre of gravity for optimal track performance.
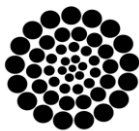
Unlike previous studies, this work focuses on the design and simulation of an independent suspension applied to a four-wheel human-powered vehicle (HPV). While other studies have focused on optimising the suspension of vehicles with engines or on unsprung structures, this work uses an innovative approach in the implementation of lightweight and commercially available materials, such as AISI 4130, together with extensive finite element analysis (FEA) and dynamic simulations in MSC ADAMS®.

The main objective is to demonstrate a significant reduction of the vertical and lateral displacement of the centre of mass of the HPV, validating the improvement in stability and manoeuvrability compared to commercial models without suspension, making this study a contribution in the field of vehicles.

Design criteria

The design of the suspension system for the human-powered vehicle (HPV), incorporated in all four wheels, must meet several essential criteria. The system should be as light as possible, selecting commercially available springs and dampers, avoiding the use of full commercial suspensions. In addition, it is required to design a coupling system to the vehicle chassis that ensures optimal integration.

It is essential to demonstrate a significant reduction in the vertical displacement of the vehicle's centre of mass in the event of road irregularities, compared to a commercial vehicle (see Figure 2) that does not have a suspension system.

Box 2

Figure 2

Go-Kart type commercial vehicle from Kart Leon products with similar characteristics to the proposed design

Methodology

Structural static analysis of the proposed chassis

To determine the material from which to propose the vehicle chassis, it is necessary to perform a finite element analysis. Srivastava et al. (2021) propose to subject the chassis to a frontal impact to assess its strength and ensure that both the material and the chassis structure will be able to withstand extreme conditions, such as severe external shocks or forces. Equation 1 is used to calculate the magnitude of the impact force, which considers that the force applied is four times the weight of the loaded vehicle, because in situations such as collisions or sudden accelerations, the forces acting on the chassis can be greater than its static weight.

$$F = m \cdot a = 4 \cdot 40 \cdot 9.81 = 1570 \, N \qquad [1]$$

The boundary conditions applied are the previously calculated force, which is applied at the front of the chassis, and a fixed support at the rear axle.

The same model was analysed with different materials, considering factors such as strength, ductility, light weight, ease of welding, ease of machining, material cost and market availability.

The three materials to be considered are AISI 1018, AISI 1020 and AISI 4130, which are most commonly used in SAE competitions; the mechanical properties of each are shown in Table 1 in green. Relevant information such as total deformation, static safety factor and Von-Mises stresses were obtained from each experiment. The values obtained are shown in Table 1 in blue.

Box 3

	MATERIAL		
	AISI 1018	**AISI 1020**	**AISI 4130**
Density (g/cc)	7.87	7.87	7.87
Yield stress (MPa)	370	294.74	460
Ultimate Effort (N/mm²)	440	394.72	560
Young's modulus (GPa)	205	210	210
Total Deformation (mm)	1.7751	1.8195	1.7328
Effort to Von-Mises Effort (MPa)	313.98	313.98	313.98
Safety factor	1.1784	0.93972	1.4651

Table 1

Mechanical properties of AISI 1018, 1020 and 4130 and simulation results for chassis design

Figure 3a and 3b show the total deformation in two tests, as an example, so that the change in deformations across the chassis as the load is applied can be seen. In both cases, the maximum deformation occurs at the front of the chassis, which is where the force is applied. With the data obtained in Table 1, it is determined that the appropriate material to use in the analysis model is AISI 4130, as it has the highest safety factor and the lowest total deformation.
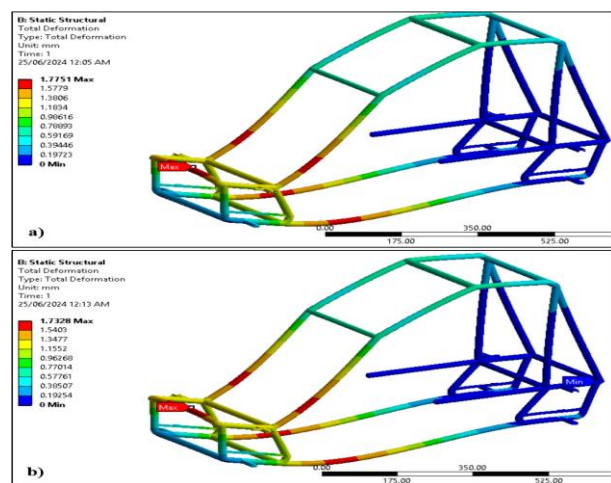
Box 4

Figure 3

a) Total deflection of the proposed chassis with material AISI 1018; b) Total deflection of the proposed chassis with material AISI 4130.

Description of the proposed suspension system

Figure 4 shows the proposed design of the suspension system.

Box 5
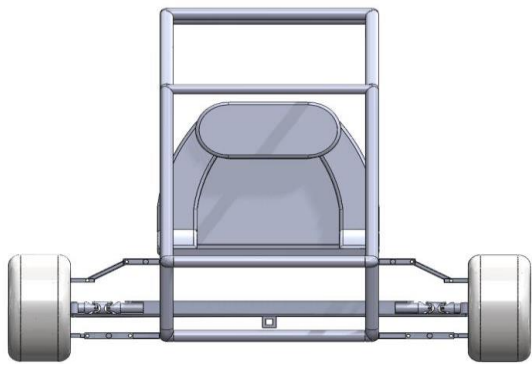
Figure 4

3D model of the proposed HPV vehicle chassis.

Figure 5a shows a more detailed picture of the suspension system, which is replicated on each wheel. The suspension system is independent and consists of two rotation joints (enclosed in red) which help to generate the longitudinal and transverse displacements; and two support mechanisms to guide the individual movement (blue), which serve as forks and join the hub carrier to the chassis, thus providing better support for the wheels.

Box 6
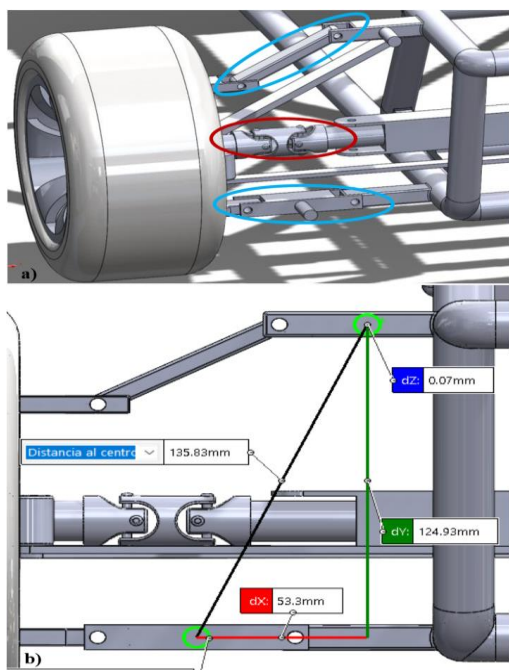
Figure 5

a) Detailed view of the suspension system;
b) Measured distance for shock absorber selection.

Shock absorber selection

To make the selection of the shock absorber, composed of the spring-shock absorber system, the distance between centres of the places destined to have the suspension, which measure 135 mm between centres, was considered, as shown in Figure 5b.

With the previous information considered, a bicycle shock absorber from the Taiwanese group, model DV-22AR marketed at DHgate, was selected (see Figure 6).

The main challenge for the designer is to find commercially available components that adequately fit the geometry of the design. In this case, the bicycle suspension measures 150 mm end-to-end, with a centre-to-centre distance of approximately 135 mm, making the shock compatible with the proposed design

Box 7

Figure 6

Selected shock absorber, model DV-22AR

Dynamic analysis in MSC ADAMS

To perform the motion analysis in ADAMS, it is important to consider the appropriate mechanical properties in each body. In this case, in addition to considering the mechanical properties of AISI 4130 steel shown in Table 1, the mechanical properties of natural rubber were also used. According to Connor (2021), the density of rubber is 110 kg/m3, Young's modulus is 0.05 GPa and Poisson's coefficient is 0.2.

Figure 7 shows the road or track where the test for the suspension system will be carried out. This road consists of a flat surface and a series of irregular bumps, which were created to observe the behaviour of the vehicle's centre of mass under a perturbation such as the one generated when passing over bumps.

Contreras-Chávez, Axel A., Pérez-Cruz, Melissa Y., Villagómez-Moreno, José and Manríquez-Padilla, Carlos G. [2024]. Design and simulation of a suspension system for a four-wheeled HPV. Journal of Technological Operations. 8[21]1-8: e3821108.
https://doi.org/10.35429/JTO.2024.8.21.3.8

Article

Box 8

Figure 7

Road to travel.

In addition, the static and dynamic coefficient of friction of the springs is considered to be μ=0.5 (Arosemena, 2024).

Description of torque and speed in the model

For the analysis of the suspension of the vehicle, a torque with a magnitude of $1\ N/m$, in a time of $t = 0.5\ s$, Afterwards, the torque is released, and at about $t = 3$ se now apply a negative torque with a value of $-1\ N/m$, which is maintained for a short period of time, until it is permanently removed. The first torque that is added to the system is to accommodate the vehicle on the track; the second torque is to give it a movement in the direction of passing the stops shown in Figure 7).
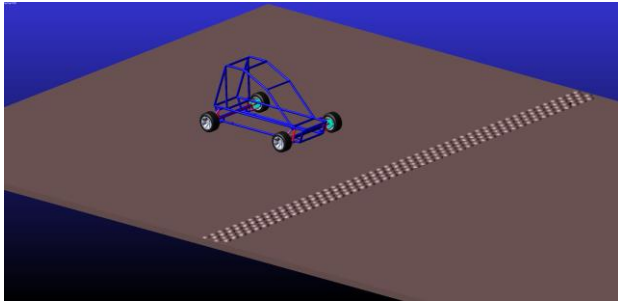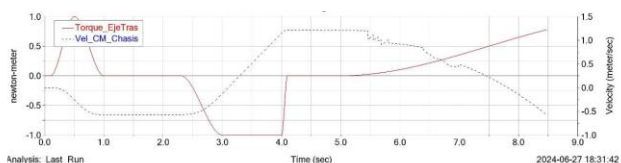
Box 9

Figure 8

Torque and Speed Graph of the proposed model

On the other hand, the speed at which the vehicle moves is of utmost importance. That is why, in Figure 8, the chassis speed graph is shown (blue dotted line). In this graph it can be seen that in the first two seconds, the vehicle acquires a negative speed, this means that the vehicle is moving backwards to accommodate itself and later, it passes from the negative to the positive frame, reaching a maximum of 1.3 m/s and its speed is maintained until it encounters obstacles in its path; this is why, from the sixth second, a distortion and decrease in the magnitude of the speed can be seen in the image, this is because the vehicle passes over the stops, decreasing its speed.

Results

To verify the proper functioning of the suspension system, the proposed model was compared with a commercial model with similar characteristics without any suspension system. Vertical and lateral displacement plots of the centre of mass of the commercial model were obtained, corresponding to the y-axis and z-axis, respectively. These plots are shown in Figure 9a and 9b, respectively.

Box 10
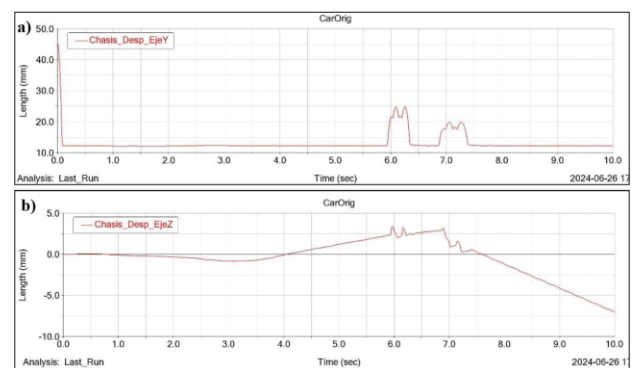
Figure 9

Vehicle displacement graph of vehicle with similar characteristics: a) on the axis *y*, b) on the axis *z*

Figure 9a shows the vertical displacement of the centre of mass, where the centre of mass remains in the same position until the vehicle suffers a disturbance (t= 6 s). These lobes refer to when the front tyres pass over the stops that were placed on the track, after a few seconds, the centre of mass suffers another alteration, due to when the rear tyres pass over the same stop. If the same figure is observed, it can be seen that the largest displacement is suffered when the front tyres manage to pass the stops, generating a displacement of the centre of mass of approximately 25 mm.

On the other hand, Figure 9b shows the lateral displacement of the centre of mass, which is equivalent to observing how the vehicle moves when facing forward. As mentioned before, at a time (t= 6 s), is when the vehicle starts to pass the bumpers; remember that this commercial vehicle does not have a shock absorber, so when faced with a perturbation such as the bumpers, every time the front or rear tyres come into contact with the bumpers, the movement of the tyres is transmitted directly to the chassis.

Contreras-Chávez, Axel A., Pérez-Cruz, Melissa Y., Villagómez-Moreno, José and Manríquez-Padilla, Carlos G. [2024]. Design and simulation of a suspension system for a four-wheeled HPV. Journal of Technological Operations. 8[21]1-8: e3821108.
https://doi.org/10.35429/JTO.2024.8.21.3.8

From the graph, it is determined that the largest displacement of the centre of mass at *axis z*, is +3.25 mm, approximately; and corresponds to the instant of time when the first tyre comes into contact with the road bumps.

To observe the behaviour of the vehicle with the proposed suspension system, the results of the displacement of the vehicle's centre of mass were also obtained, both for the y-axis and for the z-axis. This information can be seen in Figure 10a and 10b, respectively..

Box 11

Figure 10

Displacement plot of the proposed vehicle: a) on the y-axis, b) on the z-axis

In the case of the y-axis displacement, the centre of mass is not displaced until a time t= 5.5 s, which is when the front tyres start to pass the stop, and when the rear tyres meet the stones, displacement occurs again. However, the largest displacement occurs when the rear tyres pass the series of stops, thus presenting a displacement of approximately 12 mm.
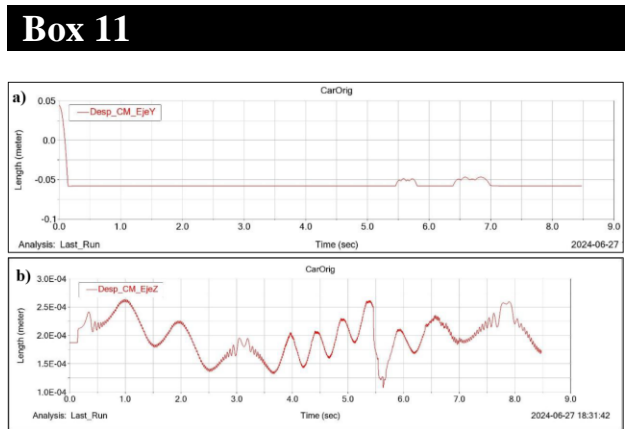
The z-axis graph has a peculiar but very interesting behaviour, as it shows the effect of a shock absorber in generating a harmonic movement. If Figure 10b is observed carefully, the magnitude of the displacement graph is relatively close to zero; in addition, the damping effect (damping coefficient) has a direct effect on the shape of this signal, as this coefficient indicates the amount of energy that can be absorbed by the system in motion.

Table 4, which contains the most relevant information from each analysis, shows the maximum displacements obtained in each experiment.

Box 12

	Maximum displacement	
	Vertical (mm)	Lateral (mm)
Vehicle Go Kart-León	25	3.25
Proposed vehicle	12	2.50E-04

Table 2

Maximum displacements in both vehicles

The most noticeable difference in the two models is the lack of a shock absorber on the commercial vehicle; therefore, when the vehicle traversed the same track as the proposed vehicle, the centre of mass shifted noticeably vertically. Numerically speaking, the displacement was almost halved with the addition of the suspension.

Conclusions

The implementation of the chassis is capable of supporting the load applied to it and the highest safety factor has a value of 1.17, under the mentioned conditions and with AISI 4130 material; which means that under a frontal impact of 4 times the magnitude of the vehicle weight, it still presents low stress magnitudes and deformations around its structure; that is why this material was chosen for the simulation of the vehicle in MSC ADAMS®.

Through the motion analysis in MSC ADAMS® it was possible to verify numerically the advantage of the created model over a commercial model, obtaining that thanks to the suspension system that the model has, the displacement of the centre of mass in the , can be reduced from 25 mm to 12 mm, which is equivalent to 52%, and in the case of the lateral displacement (), the displacement is reduced almost entirely, because the shock absorber performs the function of absorbing the energy due to the movement.

There are several opportunities to improve the design of the suspension and chassis system. One of the main areas of optimisation is the implementation of more detailed topology analysis to further reduce weight without compromising structural rigidity. In addition, the incorporation of advanced materials, such as fibre composites, could improve the strength-to-weight ratio, offering greater efficiency.

Contreras-Chávez, Axel A., Pérez-Cruz, Melissa Y., Villagómez-Moreno, José and Manríquez-Padilla, Carlos G. [2024]. Design and simulation of a suspension system for a four-wheeled HPV. Journal of Technological Operations. 8[21]1-8: e3821108
https://doi.org/10.35429/JTO.2024.8.21.3.8

Journal of Technological Operations

Article

Experimental tests to complement the simulations would also be beneficial to validate the performance of the system in real conditions and adjust the design based on the data obtained. Finally, optimisation of the damper design and its interaction with the suspension elements could lead to greater vibration absorption, further improving vehicle comfort and stability.

Declarations

Conflict of interest

The authors declare that they have no conflict of interest. They have no known competing financial interests or personal relationships that might have appeared to influence the article reported in this paper.

Author's contribution

The contribution of each researcher in each of the points developed in this research was defined on the basis of the following:

Contreras Chávez Axel Aldahir: He contributed in the conceptualisation, methodology, software, research and writing.

Pérez Cruz Melissa Yamileth: Contributed to the conceptualisation, methodology, software, research and writing.

Villagómez Moreno José: Contributed to the drafting, revision and administration of the project.

Manríquez Padilla Carlos Gustavo: Contributed to the drafting, revision and administration of the project.

Availability of data and materials

For the availability of information and material relating to this work please contact the author contact.

Funding

Acknowledgements

Abbreviations

FEA	Finite Element Analysis (Análisis por Elementos Finitos)
HPV	Human-Powered Vehicle (Vehículo de propulsión humana)

References

Background

Cebolla Bono, B. (2017). *Modelling and characterisation of suspension systems in motor vehicles* (Doctoral dissertation, Universitat Politècnica de València).

Vázquez Trevilla, N. I.(2011). *Design of vehicle suspension system formula SAE* (Doctoral dissertation, Universidad Autónoma de México).

Basic concepts

Connor, N. (2021). *Rubber | Density, strength, melting point, thermal conductivity*. Material Properties. [Online]. Revised May 2024
Srivastava, J. P., Chaithanya, B. K., Teja, K. S., Venugopal, B., Vineeth, S., Rajkumar, M., &

Khan, H. (2021). *Numerical study on strength optimization of Go-Kart roll-cage using different materials and pipe thickness*. Materials Today: Proceedings, 39, 488-492.

Arosemena, A. (n.d). *Mechanical springs*. [Online]. Revised May 2024

Supports

Auquilla Ocampo, J. L., & Torres Romero, C. R. (2016). *Design of the suspension system of an electric single-seater vehicle Formula SAE* (Bachelor's thesis).

Article

Pulido Laparra, C. (2014). *Design of the suspension system for a Formula Student vehicle.* Carlos III University of Madrid.

Differences

Gonza Valle, R. E. (2023). *Design and construction of a go-kart type vehicle with tubular structure.* Instituto Superior Tecnológico Vida Nueva.

Theoretical comparison of two shell-and-tube heat exchangers by applying different correlations

Comparación teórica de dos intercambiadores de calor de carcasa y tubos aplicando diferentes correlaciones

Huerta-Gamez, Hector[a], Hortelano-Capetillo, J. Gregorio[b], Zuñiga-Cerroblanco, J. Luis[c] and Aguilar-Moreno, A. Alberto[d]

[a] ROR Universidad Politécnica de Juventino Rosas • LUY-7745-2024 • 0000-0002-5088-310X • 373690
[b] ROR Universidad Politécnica de Juventino Rosas • LVA-2240-2024 • 0000-0002-3702-4853 • 347496
[c] ROR Universidad Politécnica de Juventino Rosas • LUY-2709-2024 • 0000-0003-0493-8197 • 208410
[d] ROR Universidad Politécnica de Juventino Rosas • LVA-2356-2024 • 0000-0002-7652-5925 • 254188

Abstract

This paper presents the theoretical analysis of heat transfer of two different shell and tube exchangers. The theoretical study was carried out with the creation of software in the EES programming the ε-NTU method, considering different correlations for the calculations of the external and internal convective coefficients as well as their geometry for each exchanger, finally performing a mass and energy balance. The theoretical results obtained in this analysis were: operating conditions at the exit of the casing and tubes, efficiencies and total heat transferred in both exchangers, the results obtained were validated with results from other researchers.

Resumen

En este trabajo se presenta el análisis teórico de la transferencia de calor de dos diferentes intercambiadores de tipo carcasa y tubos. El estudio teórico fue realizado con la creación de un software en el EES programando el método ε-NTU, considerando diferentes correlaciones para los cálculos de los coeficientes convectivos externos e interno, así como su geometría para cada intercambiador, por último, realizando un balance de masa y energía. Los resultados teóricos obtenidos en este análisis fueron: condiciones de operación a la salida de la carcasa y los tubos, eficacias y calor total transferido en ambos intercambiadores, los resultados obtenidos fueron validados con resultados de otros investigadores.

Objetives	Methodology	Contribution
Calculate the outlet temperatures of the 2 heat exchangers with different geometric configuration using different correlations for the convective coefficients and with the ε-NTU method.	The method used was the ε-NTU to calculate the outlet temperatures of the shell and tube fluids with the help of correlations to calculate the internal and external convective coefficients and obtain the overall heat transfer coefficient.	We contributed to suggesting a method for calculating the outlet temperatures where the ε-NTU method was used, different correlations for the internal and external convective coefficients, dimensions and geometries of the heat exchangers, finally validating these results with numerical simulations in CFD .

Objetivo	Metodología	Contribución
Calcular las temperaturas de salida de los 2 equipos de calor con diferente configuración geométrica usando diferentes correlaciones para los coeficientes convectivos y con el método ε-NTU con la ayuda del software EES y CFD.	El método usado fue el del ε-NTU para calcular las temperaturas de salida de los fluidos de la coraza y de los tubos con la ayuda de las correlaciones para calcular los coeficientes convectivos internos y externos y obtener el coeficiente global de transferencia de calor.	Contribuimos a sugerir un método para el calculo de las temperaturas de salida donde se utilizó el método ε-NTU, diferentes correlaciones para los coeficientes convectivos internos y externos, dimensiones y geometrías de los intercambiadores de calor, finalmente validar estos resultados con simulaciones numéricas en CFD.

Correlations, global transfer coefficient, internal and external convective coefficients, ε-NTU method
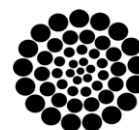
Correlaciones, Transferencia Global de Calor, Coeficientes convectivos internos y externos, ε-NTU

RENIECYT
Registro Nacional de Instituciones y Empresas Científicas y Tecnológicas
1702902 CONAHCYT

Article

Introduction

A shell-and-tube heat exchanger is equipment used to cool a fluid that is hotter than desired or vice versa. Its design is of great importance since optimal energy transfer, size and weight are often fundamental factors that affect the economy of the process.

To design or predict the performance of a heat exchanger, it is essential to relate the total heat transfer to quantities such as the overall heat transfer coefficient, which is important as it provides the total amount of heat and depends on the external and internal convective coefficients.

Yonghua You et al., [1] carried out experimental and numerical studies applying CFD to a shell-and-tube heat exchanger with flower-shaped Baffles, within their results they obtain velocity and temperature profiles, as well as the distribution of convective coefficients as a function of the Reynolds and the global calus transfer coefficients using the k-ε turbulence model.

The error percentages between the experimental and numerical data were: 8% for the external convective coefficient and 14% for the pressure drop at a velocity in the casing of 1.2 m/s. Gh. S. Jahanmir et al., [2] performed a numerical CFD simulation for a shell-and-tube heat exchanger type by varying the inclination angles of the tubes using hot and cold water as fluids, employing the RNG-k turbulence model for the analysis of pressure drops, heat transfer, global transfer coefficient and effectiveness.

The inclination angles of the tubes that present the highest performance in the exchanger are 55° and 65°, increasing heat transfer to 69% but increasing pressure drop to 23%.

Shui Ji et al., [3] show hydrodynamic and thermal simulations performed in ANSYS CFX 12.0 for 3 types of heat exchangers with the same transfer area: the first is two passes through the shell with continuous helical baffles with one passage through the tubes; the second is with a passage through the housing with a passage through the tubes and the third is with a passage through the housing with a passage through the tubes with conventional loudspeakers.

They use the k-ε turbulence model and the equations of quantity of movement and energy, showing that the first exchanger has greater heat transfer with 25%, the second exchanger has a lower pressure drop on the shell side with respect to the others. M.M. El-Fawal et al., [4] design an economic model to minimize the area of a shell-and-tube heat exchanger using correlations to calculate the convective coefficients for shell side and tube side, and use equations for the calculation of heat exchanger geometric parameters and pressure drops. Jian-Fei Zhang et al., [5] present a numerical study in CFD and experimental of a shell-and-tube heat exchanger with helical baffles under an angle of 40°, using the k-ε turbulence model with 13.5 million cells in the mesh, at the same time that the difference between the numerical and theoretical results were 25% for the pressure drop and 15% for the Nusselt number.

Quiwang Wang et al., [6] perform a numerical CFD study of a shell-and-tube heat exchanger with helical and segmented baffles, where the working fluids are hot and cold water. Under the same mass flow, the pressure drop for the exchanger with helical baffles is 13% lower and the heat transfer is 5.6% higher than the exchanger with segmented baffles. Su Thet Mon Than et al., [7] designed a software in Mathlab and Autocad for the design of a shell and tube heat exchanger, introducing the input data which are the operating conditions of the fluids on both the shell and tube sides.

They use correlations to calculate the convective coefficients for external and internal flow, applying equations for the heat exchanger's geometric calculations and pressure drops. André L. H. Costa et al., [8] presents the minimization of the surface area of a shell and tube heat exchanger using genetic algorithms and the LMTD method, the input data are the operating conditions of the fluids and geometric data of the heat exchanger to obtain the minimum area for said process; In addition, they do not use correlations for the calculation of the global transfer coefficient.

Uday C. Kapale et al., [9] propose a model to calculate the pressure drop on the side of the casing as a function of the cut of the baffle and the arrangement of the tubes that are subsequently compared with experimental results.

The fluids used for the model were water and oil with a Reynolds of 1x103 to 1x105 obtaining an error percentage of 2.4 to 4% with oil and 2.8 to 7.4% with water. K.C. Leong et al., [10] designed software in Delphis Programming Languaje for the design of a shell and tube heat exchanger, the input data is the operating conditions of the inlet and outlet fluids; for the calculation of the convective coefficient and the pressure drop on the shell side, they used the Bell Delaware method but do not present correlations for the convective coefficients on the tube side.

Methodology

For the model generated in the EES, the input parameters are: geometric data of the heat exchanger, mass flows, temperatures and inlet pressures of the casing and tubes. In the simulation model, the thermal properties of the fluids are determined and a calculation algorithm is applied to determine the output operating conditions of the shell and tube heat exchanger.

Four correlations were used for the analysis of internal and external flow, for internal flow are: Colburn, Petukov-Kirillov, Dittus Boelter and Gnielinski; for external flow are: Zukauskas, Kern, Hilpert and Taborek for turbulent flow conditions without phase change.

Internal Flow

The convective coefficient of heat transfer can be determined with a correlation for Nusselt's number, Colburn [11] with a Re>10000:

$$Nu_D = \frac{h_i D_{int}}{k} = 0.023 \, Re_D^{4/5} \, Pr^{1/3} \qquad [1]$$

The Dittus-Boelter [12] correlation is a slightly different version than that of Colburn with a Re>10000:

$$Nu_D = \frac{h_i D_{int}}{k} = 0.023 \, Re_D^{4/5} \, Pr^{0.4} \qquad [2]$$

The following expression is proposed by Gnielinski [13], where all properties are evaluated at the mean temperature with a Reynolds interval between 3000<Re<5x106:

$$Nu_D = \frac{h_i D_{int}}{k} = \frac{\left(\frac{f}{8}\right)[Re_D - 1000]Pr}{1 + 12.7\left(\frac{f}{8}\right)^{1/2}\left(Pr^{2/3} - 1\right)} \qquad [3]$$

$$f = (0.79 Ln\,Re_D - 1.64)^{-2}$$

The expression proposed by Petukov-Kirillov [14], shows a more complex form for this analysis, involving a friction factor but which in turn has a lower error compared to that of Dittus Boelter and Colburn, with a D>2100:

$$Nu_D = \frac{h_i D_{int}}{k} = \frac{\left(\frac{f}{2}\right)Re_D \, Pr}{1.07 + 12.7\left(\frac{f}{2}\right)^{1/2}\left(Pr^{2/3} - 1\right)} \qquad [4]$$

$$f = (1.58 Ln\,Re_D - 3.8)^{-2}$$

The Reynolds number is defined as:

$$Re_D = \frac{u \cdot \rho \cdot D_{int}}{\mu} \qquad [5]$$

And Prandtl's number is:

$$Pr = \frac{\mu \cdot Cp}{k} \qquad [6]$$

External Flow

The correlation of Zukauskas [15] is determined by the following expression:

$$Nu_D = \frac{h_o D_{ext}}{k} = C \, Re_D^m \, Pr^{0.6}\left(\frac{Pr}{Pr_s}\right)^{1/4} \qquad [7]$$

Where the coefficients "C" and "m" can be estimated according to the Reynolds number:

$$10 < Re \leq 100 \rightarrow C = 0.9, m = 0.4$$
$$100 < Re \leq 1000 \rightarrow C = 0.683, m = 0.466$$
$$1000 < Re \leq 2x10^5 \rightarrow C = 0.35, m = 0.65$$

The estimation of the Reynolds number comes from the previous knowledge of the flow velocity, this in turn of a passage area involving the geometric characteristics of the exchanger, is expressed by the following equation:

Huerta-Gamez, Hector, Hortelano-Capetillo, J. Gregorio, Zuñiga-Cerroblanco, J. Luis and Aguilar-Moreno, A. Alberto. [2024]. Theoretical comparison of two shell-and-tube heat exchangers by applying different correlations. Journal of Technological Operations. 8[21]1-11: e4821111.
https://doi.org/10.35429/JTO.2024.8.21.1.11

Article

$$A_{paso} = \left[\frac{L_{carc}}{N_{baf}+1}\right]\left[D_{intarc} - \left(\frac{D_{intarc}}{P_t}-1\right)D_{ext}\right] \quad [8]$$

Another methodology of analysis for the external convective coefficient on an array of tubes is proposed by Kern [16], based on an equivalent diameter, applying the following correlation:

$$\frac{h_o D_e}{k_c} = 0.36\left(\frac{D_e G_s}{\mu_c}\right)^{0.55}\left(\frac{Cp_c \mu_c}{k_c}\right)^{\frac{1}{3}}\left(\frac{\mu_c}{\mu_w}\right) \quad [9]$$

Where, Gs, is the mass velocity of the fluid on the casing side and the properties are evaluated at medium temperature; The equivalent diameter for a triangular array is obtained as follows:

$$D_e = \frac{4\left(\frac{P_t^2 \sqrt{3}}{4} - \frac{\pi D_{ext}}{8}\right)}{\frac{\pi D_{ext}}{2}} \quad [10]$$

The magnitude of the mass velocity, Gs, can be defined over an area of cross-flow arrangement, represented by an area for maximum flow. It is obtained by the following expression:

$$G_s = \frac{m_{carc}}{A_s} \quad [11]$$

$$A_s = \left[1 - \frac{D_{ext}}{P_t}\right]D_{intarc}\left(\frac{L_{carc}}{N_{baf}+1}\right) \quad [12]$$

Another method for the convective coefficient is proposed by Taborek [17], where the Reynolds number is based on the diameter of the tubes and the velocity of the fluid over the cross-flow area of the carcass diameter.

$$Nu_D = \frac{h_o D_{ext}}{k} = 0.2\,\text{Re}_s^{0.6}\,\text{Pr}^{0.4} \quad [13]$$

$$\text{Re}_s = \frac{m_{carc} D_{ext}}{A_s \mu}$$

Hilpert's correlation [18]:

$$Nu_D = C Re_D^m Pr^{0.33} \quad [14]$$

Re_D	C	m
0.4–4	0.989	0.330
4–40	0.911	0.385
40–4000	0.683	0.466
4000–40,000	0.193	0.618
40,000–400,000	0.027	0.805

Representing the global coefficient with the internal and external convection phenomena, the following equation [19] is obtained:

$$U = \frac{1}{\dfrac{D_{ext}}{D_{int}h_i} + \dfrac{D_{ext}Ln\left(D_{ext}/D_{int}\right)}{2k_{mat}} + \dfrac{1}{h_o}} \quad [15]$$

The total heat transfer area can also be formulated in terms of the length of the tubes, number of tubes and the inner diameter of the tubes.

$$A_{total} = \pi D_{int} L N_{tub} \quad [16]$$

The thermal analysis is based on the ε-NTU method, the efficacy and NTU is estimated as follows,

$$NTU = \frac{UA_{total}}{C_{min}} \quad [17]$$

Effectiveness is determined by considering countercurrent flow:

$$\varepsilon = \frac{1 - \exp\left[-NTU(1-Cr)\right]}{1 - Cr\exp\left[-NTU(1-Cr)\right]} \quad [18]$$

$$Cr = \frac{C_{min}}{C_{max}}$$

To calculate the total heat of the heat exchanger is determined as a function of efficiency, minimum capacitance and fluid inlet temperatures, as expressed in the following equation:

$$Q_{max} = \varepsilon \cdot C_{min}(T_{ec} - T_{et}) \quad [19]$$

Once the total heat is determined, the outlet temperatures of the casing-side and tube-side fluids can be estimated using an energy balance as shown in the following equation:

$$Q_{total} = m_{carc}Cp_{carc}(T_{sc} - T_{ec})$$ [20]
$$Q_{total} = m_{tubos}Cp_{tubos}(T_{et} - T_{st})$$

The pressure drop on the side of the tubes is calculated with the following equation [20]:

$$\Delta P_t = \left(\frac{4fLNp}{Di_{tub}} + 4Np\right)\left(\frac{\rho v^2}{2}\right)$$ [21]

$$f = (0.79 LnRe_D - 1.64)^{-2}$$

For the Shell side, the following equation is used [20]:

$$\Delta P_s = \frac{fG_s^2(Nb+1)D_s}{2\rho D_e\left(\frac{\mu}{\mu_w}\right)^{0.14}}$$ [22]

$$f = \exp(0.576 - 0.19 LnRe_s)$$

To validate the model proposed in this work, a simulation was carried out in the EES software, varying the mass flows at different inlet temperatures, while the mass flow and the temperature of the mixture remain constant

Table 1 shows the geometric parameters that are required to obtain the results of the internal and external convective coefficients, the total heat transfer area and the pressure drops of both the shell or shell side and the tube side.

Box 1

Table 1

Geometric data of the heat exchanger

| Internal diameter of the tubes. |
| Extenal diameter of the tubes. |
| Number of bafles |
| Number of tubes. |
| Length of tubes |
| Radio Pitch |
| Number of tube steps |
| Material conductivity |

Source Own.

The shell-and-tube type heat exchangers shown in Figure 1 are designed to heat water with a simple and flexible installation. Heat exchangers can be connected to a boiler, heat pump, solar panel systems, or other heat source. The working fluids are cold water at the inlet on the tube side and hot water on the shell side.

Box 2
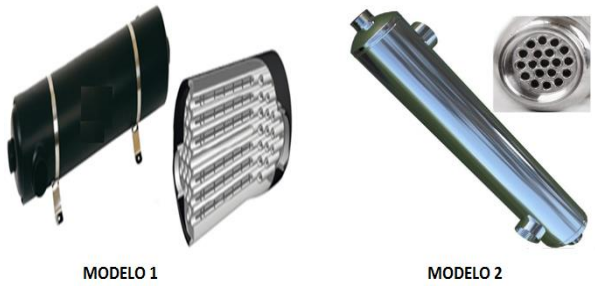
Figure 1

Shell and Tube Heat Exchangers

Source Own.

Table 2 shows the geometric data of model 1 with a transfer area of 2.65 m^2 proposed to carry out the present study and model 2 with a transfer area of 2.96 m^2.

Box 3

Table 2

Geometric data of the exchanger, shell and tubes, design 1 and 2

	Design1	Design 2
Length of the tubes (m)	1.2	1.6
Outer diameter of tubes (m)	0.02	0,031
Inner diameter of the tubes (m)	0.019	0.03
Number of Shell Steps	1	1
Number of baffles	6	8
Number of tube passes	1	1
Number of tubes	37	19
Distance between tube centers (m)	0.05	0.045

Figures 2 and 3 show a window of the program where the geometric parameters of the equipment, volumetric flow, the inlet temperatures of both fluids, and the geometric data of the heat exchanger are entered.

The simulation model determines the thermal properties of the fluids and applies a calculation algorithm to determine the output operating conditions of the shell-and-tube heat exchanger.

Box 4
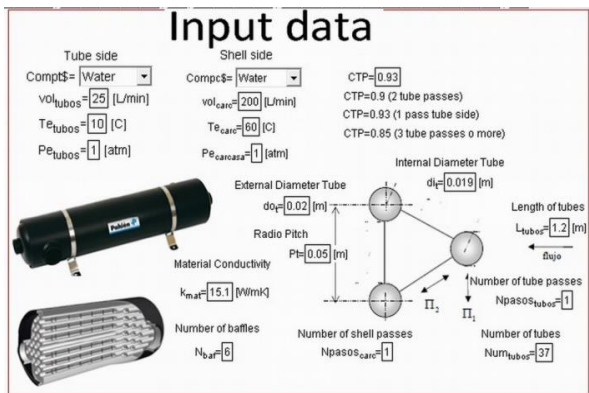
Figure 2

Shell and Tube Heat Exchangers 1

Source Own.

Box 5
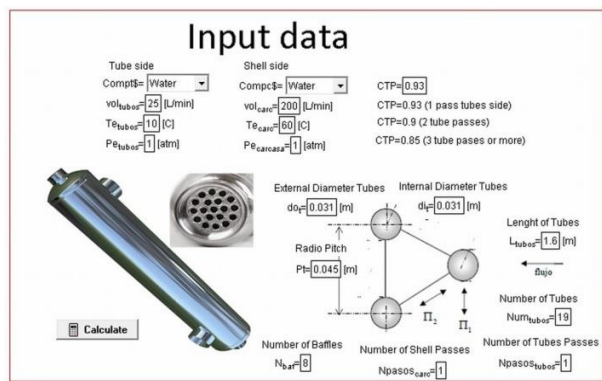
Figure 3

Shell and Tube Heat Exchangers 2

Source Own

Table 3 shows the volumetric flows and inlet temperatures of both fluids from the 3 simulations, then make comparisons of the results. It is observed that the flow on the side of the tubes is 25 L/min and on the side of the shell is 200 L/min, the 3 simulations show the different inlet temperatures.

The numerical study of the flow developed over a shell and tube heat exchanger requires a mathematical presentation of the turbulent motion of the fluid, which in turn can be transformed into an algorithm for its solution. This mathematical representation is summarized in a set of equations for the conservation of mass, momentum and energy; as well as the k-ε turbulence model [21].

Box 6

Table 3

Input data of volumetric flows and temperatures from the 3 simulations with the EES software

Shell side (L/min)	200
Tubes side (L/min)	25

Simulation 1		Simulation 2		Simulation 3	
Tet ºC	10	Tet ºC	20	Tet ºC	10
Tec ºC	60	Tec ºC	70	Tec ºC	45

The CFD preprocessor is used to create the geometry and meshing of the heat exchanger. Figures 4 and 5 show the geometries of the exchangers whose meshes are composed of 4 million nodes with tetrahedral elements to represent the computational domain. The computational process is carried out by applying boundary conditions such as temperature and inlet mass flows for both fluids to solve the 3D model with double precision.

Box 7
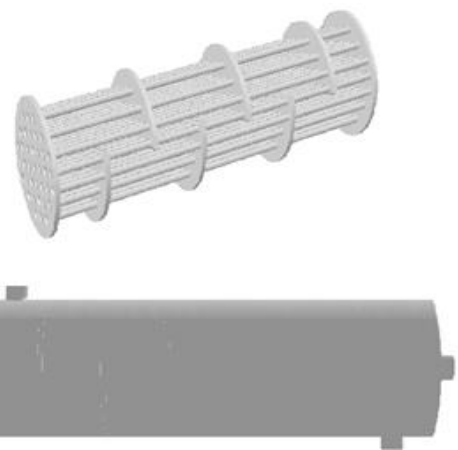
Figure 4

Shell and Tube Heat Exchangers 1

Box 8

Figure 5

Huerta-Gamez, Hector, Hortelano-Capetillo, J. Gregorio, Zuñiga-Cerroblanco, J. Luis and Aguilar-Moreno, A. Alberto. [2024]. Theoretical comparison of two shell-and-tube heat exchangers by applying different correlations. Journal of Technological Operations. 8[21]1-11: e4821111.
https://doi.org/10.35429/JTO.2024.8.21.1.11

Article

Results

Simulation 1

Table 4 shows the results of simulation 1, showing the results comparisons of the outlet temperatures with the different combinations of correlations.

Box 9

Table 4

Results of simulation 1 of model 1 in EES software

Simulation 1			
	Design 1		
hi (W/m-K)		ho(W/m-K)	ΔP Tubes (Pa)
Petukov	535.4	Zukauskas 548.1	64.19
Colburn	409	Hilpert 576	ΔP Shell (Pa)
Gnielinski	72.83	Taborek 1881	103.4
Dittus Boelter	479.3	Kern 1097	
		U (W/m-K) Q(W)	Efficiency (E)
Dittus Boelter-Zukauskas		246.6 26722	0.3
Gnielinski-Kern		64.94 8146	0.1
Petukov-Taborek		395 35247	0.43
Gnielinski-Zukauskas		61.31 7713	0.08
Colburn-Hilpert		230.2 25265	0.29
		Tst Tsc	
Dittus Boelter-Zukauskas		25.32 58.08	
Gnielinski-Kern		14.67 59.41	
Petukov-Taborek		31.92 57.21	
Gnielinski-Zukauskas		14.62 59.44	
Colburn-Hilpert		24.48 58.16	

Figure 6 and Table 5 shows the temperature results and heat transfer contours of model 1 as a result of simulation 1. The temperature changes are observed on the shell side where the change is smaller, the hot fluid enters at 60 ºC (333 K) and exits at 57.29 ºC (330.29 K); on the other hand, the cold fluid enters at 10 ºC (283 K) and exits at 31.64 ºC (304.64 K) observing that the temperature change was greater inside the tubes.

Box 10

Cv
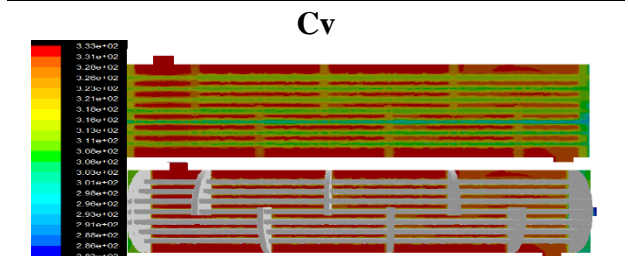
Figure 6

Figure 7 shows the flow path on the shell side as it passes through the exchanger where it can be seen that there is no stagnation near the baffles, which is very important for more effective heat transfer.

Box 11

Figure 7

Shell and Tube Heat Exchangers 1. Flow trayectories

Source Own.

Box 12

Table 5

Results of simulation 1 for the model 1 in CFD.

	CFD
Tst ºC	31.64
Tsc ºC	57.29

The numerical and theoretical results of simulation 1 for the model 1, where the inlet temperature on the tube side is 10 °C and on the shell side 60 °C, are shown. It is observed that the theoretical results obtained with the combinations of the Petukov-Taborek coefficients are close to the numerical results in CFD.
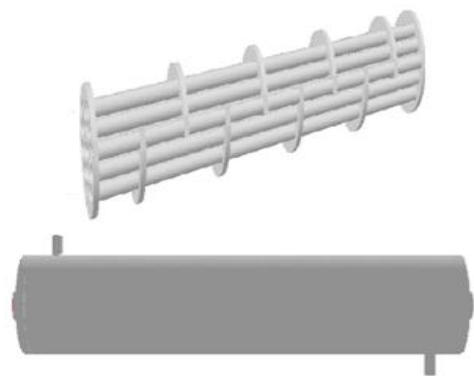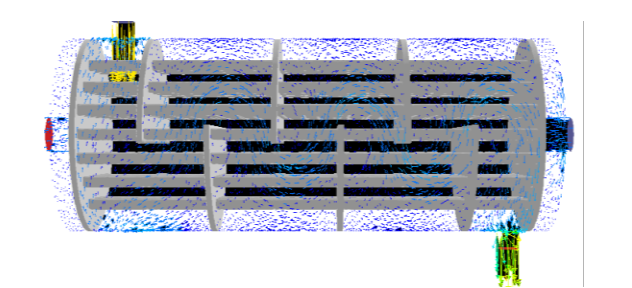
Table 6 shows the results of simulation 1, showing the results comparisons of the outlet temperatures with the different combinations of correlations.

Box 13

Table 6

Results of simulation 1 of model 2 with the EES software

Simulation 1			
	Design 2		
hi (W/m²-K)		ho(W/m²-K)	ΔP Tubes (Pa)
Petukov	397.7	Zukauskas 1737	32.16
Colburn	306.6	Hilpert 1862	ΔP Shell (Pa)
Gnielinski	120.2	Taborek 2313	528
Dittus Boelter	359.9	Kern 1958	
		U (W/m²-K) Q (W)	Efficiency (E)
Dittus Boelter-Zukauskas		286.7 32795	0.376
Gnielinski-Kern		109.4 14625	0.166
Petukov-Taborek		326.4 36108	0.41
Gnielinski-Zukauskas		107.8 14532	0.166
Colburn-Hilpert		253.6 29832	0.34
		Tst Tsc	
Dittus Boelter-Zukauskas		28.8 57.61	
Gnielinski-Kern		18.38 58.93	
Petukov-Taborek		30.7 57.3	
Gnielinski-Zukauskas		18.33 58.94	
Colburn-Hilpert		27.1 57.82	

Huerta-Gamez, Hector, Hortelano-Capetillo, J. Gregorio, Zuñiga-Cerroblanco, J. Luis and Aguilar-Moreno, A. Alberto. [2024]. Theoretical comparison of two shell-and-tube heat exchangers by applying different correlations. Journal of Technological Operations. 8[21]1-11: e4821111.
https://doi.org/10.35429/JTO.2024.8.21.1.11

Journal of Technological Operations

Article

Figure 8 shows the temperature contours and velocity profiles of the fluid in model 2 as a result of simulation 1. It can be seen that the temperature of the hot fluid decreases slightly to 57.26 ºC (330.26 K), but the cold fluid exits at 29.31 ºC (302.31 K). Making a numerical comparison between the two exchangers, the outlet temperature of the cold fluid is higher than in model 2. It can also be seen that the mass flow path from the shell side flows without any problem along the exchanger as shown in Figure 9. Making a comparison between theoretical and numerical results, it is observed that the combinations of Petukov-Taborek, Dittus Boelter-Zukauskas and Colburn-Hilpert correlations approximate the CFD results in the Table 7.
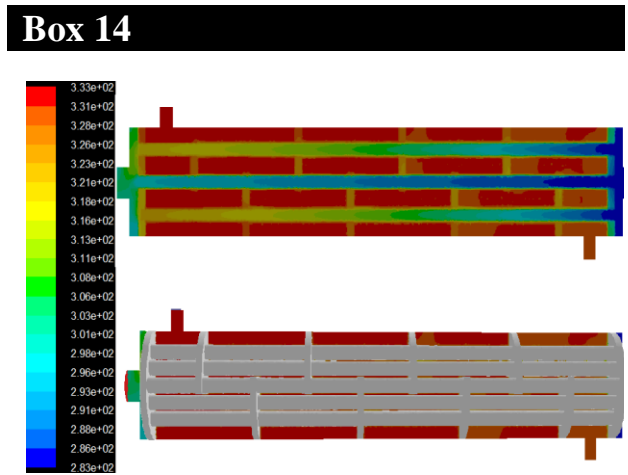
Box 14

Figure 8

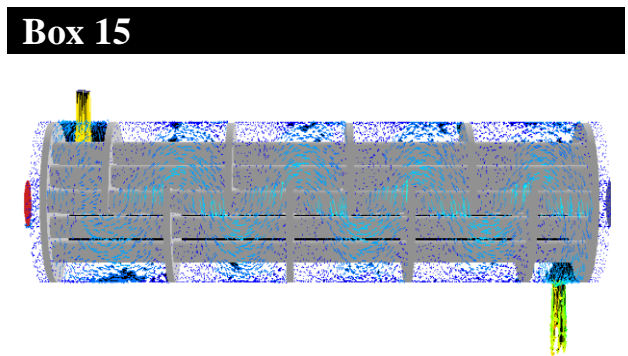Shell and Tube Heat Exchangers 2. Temperature contours in K.

Source Own.

Box 15

Figure 9

Shell and Tube Heat Exchangers 2.Flow trayectorie

. *Source Own*

Box 16

Table 7

Results of simulation 1 for the model 2 in CFD

	CFD
Tst ºC	29.31
Tsc ºC	57.26

Simulation 2

Table 8 shows the results of simulation 2 on design 1 using the different correlations; Table 9 shows the CFD results. The CFD results are 39.5 ºC for the tube side and 67.5 ºC for the shell side.

The outlet temperatures obtained with the combination of Dittus Boelter-Zukauskas correlations were 36.84 ºC for the tube side and 67.5 ºC for the shell side, these results are close to those of the CFD results.

Box 17

Table 8

Results of simulation 2 of model 1 with the EES software

Simulation 2					
		Design 1			
h_i(W/m²-K)		h_o(W/m²-K)		ΔP Tubes (Pa)	
Petukov	611.2	Zukauskas	611.7	59	
Colburn	472.7	Hilpert	604	ΔP Shell (Pa)	
Gnielinski	208.3	Taborek	1945	99.54	
Dittus Boelter	542.5	Kern	1146		
		U(W/m²-K)	Q(W)	Efficiency (E)	
Dittus Boelter-Zukauskas		277.1	29303	0.33	
Gnielinski-Kern		167.8	19344	0.22	
Petukov-Taborek		440.5	41217	0.47	
Gnielinski-Zukauskas		148.8	17415	0.2	
Colburn-Hilpert		255.3	27460	0.31	
		Tst ºC	Tsc ºC		
Dittus Boelter-Zukauskas		36.84	67.85		
Gnielinski-Kern		31.12	68.58		
Petukov-Taborek		43.7	67		
Gnielinski-Zukauskas		30	68.7		
Colburn-Hilpert		35.78	68		

Box 18

Table 9

Results of simulation 2 for the model 1 in CFD

	CFD
Tst ºC	39.5
Tsc ºC	67.5

Huerta-Gamez, Hector, Hortelano-Capetillo, J. Gregorio, Zuñiga-Cerroblanco, J. Luis and Aguilar-Moreno, A. Alberto. [2024]. Theoretical comparison of two shell-and-tube heat exchangers by applying different correlations. Journal of Technological Operations. 8[21]1-11: e4821111.
https://doi.org/10.35429/JTO.2024.8.21.1.11

Journal of Technological Operations

Article

Tables 10 and 11 show the results of simulation 2 on design 2. The CFD results obtained for the outlet temperatures were 41 on the tube side and 67 on the shell side.

The results obtained with the combination of correlations of the outlet temperatures and approximated the numerical ones were Dittus Boelter-Zukauskas (40.6 on the tube side and 67.37 $^{\circ}$C on the shell side) and Petukov-Taborek (42.53 $^{\circ}$C on the tube side and 67.13 $^{\circ}$C on the shell side).

Box 19
Table 10

Results of simulation 2 of model 2 with the EES software.

Simulation 2				
Design 2				
hi (W^2/m-K)		ho(W/^{2}m-K)		ΔP Tubes (Pa)
Petukov	454.1	Zukauskas	1939	29.81
Colburn	354.1	Hilpert	1951	ΔP Shell (Pa)
Gnielinski	213.1	Taborek	2393	508.3
Dittus Boelter	406.3	Kern	2045	
		U (W/m^2-K)	Q (W)	Efficiency (E)
Dittus Boelter-Zukauskas		323.4	35837	0.41
Gnielinski-Kern		186.2	23214	0.26
Petukov-Taborek		366.7	39205	0.45
Gnielinski-Zukauskas		185.2	23117	0.26
Colburn-Hilpert		288.6	32936	0.378
		Tst $^{\circ}$C	Tsc $^{\circ}$C	
Dittus Boelter-Zukauskas		40.6	67.37	
Gnielinski-Kern		33.34	68.3	
Petukov-Taborek		42.53	67.13	
Gnielinski-Zukauskas		33.29	68.31	
Colburn-Hilpert		39	67.59	

Box 20
Table 11

Results of simulation 2 for the model 2 in CFD

	CFD
Tst $^{\circ}$C	41
Tsc $^{\circ}$C	67

Simulation 3

Tables 12 and 13 show the results obtained in simulation 3 with design 1. The results obtained in CFD are close to the results obtained with the Petukov-Taborek correlations.

Box
Table 12

Results of simulation 3 of model 1 with the EES software.

Simulation 3				
Design 1				
hi (W/m^2-K)		ho(W/m^2-K)		ΔP Tubes (Pa)
Petukov	535.4	Zukauskas	473.9	64.19
Colburn	409	Hilpert	529.7	ΔP Shell (Pa)
Gnielinski	72.83	Taborek	1770	107.6
Dittus Boelter	479.3	Kern	1038	
		U(W/m^2-K)	Q(W)	Efficiency (E)
Dittus Boelter-Zukauskas		230.4	17699	0.29
Gnielinski-Kern		64.72	5684	0.1
Petukov-Taborek		389.9	26531	0.43
Gnielinski-Zukauskas		60.25	5311	0.09
Colburn-Hilpert		222.4	17195	0.28
		Tst $^{\circ}$C	Tsc$^{\circ}$C	
Dittus Boelter-Zukauskas		20.15	43.72	
Gnielinski-Kern		13.26	44.59	
Petukov-Taborek		25.21	43	
Gnielinski-Zukauskas		13	44.62	
Colburn-Hilpert		19.86	43.75	

Box
Table 13

Results of simulation 3 for the model 1 in CFD.

	CFD
Tst $^{\circ}$C	26.7
Tsc $^{\circ}$C	42.3

Tables 14 and 15 show the results obtained in simulation 3 with design 2. The results obtained in CFD are close to the results obtained with the Petukov-Taborek and Dittus Boelter-Zukauskas correlations.

Box
Table 14

Results of simulation 3 of model 2 with the EES software.

Simulation 3				
Design 2				
hi (W/m^2-K)		ho(W/m^2-K)		ΔP Tubes (Pa)
Petukov	397.7	Zukauskas	1502	32.16
Colburn	306.3	Hilpert	1712	ΔP Shell (Pa)
Gnielinski	120.2	Taborek	2177	549.6
Dittus Boelter	359	Kern	1852	
		U (W/m^2-K)	Q (W)	Efficiency (E)
Dittus Boelter-Zukauskas		279.5	22520	0.37
Gnielinski-Kern		109.1	10209	0.16
Petukov-Taborek		323.5	25119	0.41
Gnielinski-Zukauskas		107.6	10084	0.16
Colburn-Hilpert		250.6	20693	0.33
		Tst $^{\circ}$C	Tsc $^{\circ}$C	
Dittus Boelter-Zukauskas		22.91	43.37	
Gnielinski-Kern		15.85	44.26	
Petukov-Taborek		24.4	43.18	
Gnielinski-Zukauskas		15.78	44.27	
Colburn-Hilpert		21.86	43.5	

Huerta-Gamez, Hector, Hortelano-Capetillo, J. Gregorio, Zuñiga-Cerroblanco, J. Luis and Aguilar-Moreno, A. Alberto. [2024]. Theoretical comparison of two shell-and-tube heat exchangers by applying different correlations. Journal of Technological Operations. 8[21]1-11: e4821111.
https://doi.org/10.35429/JTO.2024.8.21.1.11

Box

Table 15

Results of simulation 3 for the model 2 in CFD

	CFD
Tst ºC	25.64
Tsc ºC	43.06

Conclusions

The results of the outlet temperatures of both fluids obtained with the Petukov-Taborek correlation combinations fit well with the numerical results in CFD for the proposed heat exchanger models. However, with the other combinations of correlations good results were not obtained because the internal Gnielinski and Colburn convective coefficients turned out to have very small values which did not fit any combination with the external coefficients.

The causes that affected these results were Reynolds number and the thermal properties evaluated at the operating temperatures of the exchanger, which shows that not all correlations are adjustable to the heat exchanger models. Numerical simulation was very important, since it helped to obtain reliable results from the heat exchangers and to validate the theoretical results using different correlations.

Meshing was essential, the finer the mesh, the more reliable the results, but a computing resource with a large capacity is also required to perform the modeling. Both heat exchanger models proposed to heat the water in a swimming pool are adequate; However, model 1 is more effective than model 2. When cold water enters both exchangers at the same temperature, in model 1 it comes out hotter than in model 2, with a difference of approximately 2 degrees.

Conflict of interest

The authors declare no interest conflict. They have no known competing financial interests or personal relationships that could have appeared to influence the article reported in this article.

References

Differences

[1] YonghuaYou., Aiwu Fan., Suyi Huang., Wei Liu., (2012) *"Numerical modeling and experimental validation of heat transfer and flow resistence on the shell side of a shell-and-tube heat exchanger with flower baffles"* International Journal of Heat and Mass Transfer.

[2] Gh. S. Jahanmir., F. Farhadi., (2012) *"Twisted bundle heat exchanger performance evaluation by CFD (CJ12/5054)"* International Communications in Heat and Mass Transfer.

[3] Shui Ji.,Wen-Jing Du., Peng Wang., Lin Cheng., (2011) *"Numerical Investigation on Double Shell-Pass Shell-and-Tube Heat Exchanger with Continuos Helical Baffles"* Journal of Thermodynamics.

[4] M.M. El-Fawal., A. A. Fahmy., B. M. Taher., (2011), *"Modelling of Economical Design of Shell and Tube type Heat Exchanger using Specified pressure drop".* Journal of American Science. 2011;7(12).

[5] Jian-Fei Zhang., Ya-Ling He., Wen-Quan Tao., (2009*) "3D numerical simulation on shell-and-tube heat exchanger with middle-overlapped helical baffles and continuous baffles. Part I: Numerical model and results of whole heat exchanger with middle-overlapped baffles."* International Journal of Heat and Mass Transfer.

[6] Qiuwang Wang., Qiuyang Chen., Guidong Chen., Min Zeng., (2009) *"Numerical investigation on combined multiple shell-pass and tube heat exchanger with continuous helical baffles"* International Journal of Heat and Mass Transfer.

[7] Su Thet Mon Than.,Khin Aung Lin., M. Sandar Mon., (2008), *"Heat Exchanger Desing"*, World Academy of Science, Engineering and Technology 46.

[8] André L. H. Costa., Eduardo M. Quiroz., (2008), *"Design Optimization of Shell and Tube Heat Exchanger",* Applied Thermal Engineering.

[9] Uday C. Kapale., Satish Chand., (2006) *"Modeling for shell-side pressure drop for liquid flow in shell-and-tube heat exchanger"* International Journal of Heat and Mass Transfer.

[10] K. C. Leong., K. C. Toh., Y.C. Leong., (1998*), "Shell and Tube Heat Exchanger Design Sofware for Educational Applications".* International Journal of Engineering Education.

Basics

[11] Colburn A. P., (1933), Trans, AIChE, 29, 174.

[12] Dittus F. W., Boelter L. M. K., (1930), University of California Berkeley, *Publications on Engineering, vol 2.*

[13] Gnielinski U., (1976), *"New Equations for Heat and Mass Transfer in turbulent pipe and channel flow"*. Int. Chem. Eng. Vol. 16, 359-368.

[14] Petukov B. S., (1976), *"Heat Transfer and friction in turbulent pipe flow with variable physical properties"*. In advances in Heat Transfer, Vol.6, 504-564, Academic New York.

[15] Zukauskas A. A., (1987), *"Convective Heat Transfer in cross flow, in Handbook of single-phase convective Heat Transfer"*. S. Kakac, R. K. Shah and W. Aung (Eds), 6.1-6.45 Wiley New York.

[16] Kern D. Q., (1950), *Process Heat Transfer*, McGraw Hill, New York.

[17] Taborek J., (1983), *"Shell and Tube Heat Exchanger in Heat Exchanger Desing"* Handbook, E.U. Schlünder (Ed). Section 3.3. Hemisphere, New York.

[18] Hilpert R. Forsch. Geb. Ingenieurwes., 4, 215, 1933.

[19] Incropera, De Witt, Bergman, Lavine. *Fundamentals of Heat and Mass Transfer.Sixth Edition.*

[20] Kakac S. Liu H. Heat Exchanger Selection, Rating and thermal desing. 1998. By CRC Press LLC.

[21] V. Yakhot and L. M. Smith, *"The renormalization group, the ε-expansion and derivation of turbulence models,"*Journal of Scientific Computing, vol. 7, no. 1, pp. 35–61, 1992.

Grid-interconnected photovoltaic system as an alternative to achieve climate neutrality through the energy transition

Sistema Fotovoltaico Interconectado a la red, como alternativa para lograr la neutralidad climática a través de la transición energética

Marroquín de Jesús Ángel [a], Castillo-Martínez, Luz Carmen [b], Soto-Álvarez, Sandra [c] and Olivares-Ramírez, Juan Manuel [d]

[a] ROR Universidad Tecnológica de San Juan del Río• 0000-0001-7425-0625 •81204
[b] ROR Universidad Tecnológica de San Juan del Río• 0000-0001-7953-0431
[c] ROR Universidad Tecnológica de San Juan del Río
[d] ROR Universidad Tecnológica de San Juan del Río • 0000-0003-2427-6936

Abstract

This work is based on the methodology proposed by the International Renewable Energy Agency (IRENA) as the methodology to be followed by a certified designer of photovoltaic systems. It shows the calculations to select the electrical protections, the calibers of the phase and ground conductors, channeling and distribution board, the photovoltaic system has been in operation for about four years, using the inverter manufacturer's platform, it is possible to obtain information related to the number of tons of CO_2 that has been stopped emitting to the atmosphere as well as the total energy generated.

Resumen

El presente trabajo está basado en la metodología propuesta por la Agencia Internacional de Energías Renovables (IRENA) como metodología a seguir por un diseñador certificado de sistemas fotovoltaicos. Muestra los cálculos para seleccionar las protecciones eléctricas, los calibres de los conductores de fase y de tierra, canalizaciones y tablero de distribución, el sistema fotovoltaico ha estado en operación por alrededor de cuatro años, utilizando la plataforma del fabricante de los inversores, es posible obtener información relacionada con el número de toneladas de CO_2 que se ha dejado de emitir a la atmósfera de igual manera el total de energía generada..
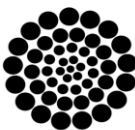
Renewable energies, Solar energy, Photovoltaic systems, Photovoltaic power plants, Distributed generation
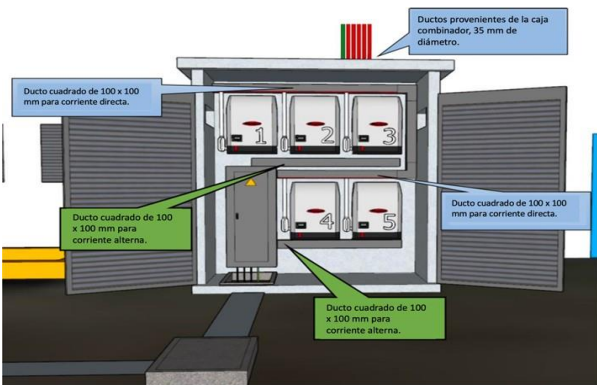
Energías renovables, Energía solar, Sistemas fotovoltaicos, Plantas fotovoltaicas, Generación distribuida

RENIECYT
Registro Nacional de Instituciones y Empresas Científicas y Tecnológicas
1702902 CONAHCYT

Journal of Technological Operations

Article

Introduction

The main components of a photovoltaic system connected to the grid are: the photovoltaic array, which is the element in charge of transforming the sun's radiation into electricity; and a power conditioning element, a direct current to alternating current inverter, whose function is to adapt the energy generated by the array to the electrical characteristics of the grid to which it will be connected.

A PV array is made up of a number of arrays or PV power sources. The number of units will depend on the nominal power required in the array and the peak power of the selected modules. The output voltage of the array, which corresponds to the operating voltage of the inverter, is obtained by connecting a number of arrays or PV power sources in series, and the power is obtained by connecting them in parallel. Currently, the nominal power of solar photovoltaic modules or panels is 570 Wp. The typical efficiency of these modules under standard irradiance and temperature conditions (i.e., 1,000W/m2) is between 14 and 22% for monocrystalline polycrystalline silicon (25°C, AM 1.5) and between 5 and 7% for amorphous silicon.

The most important potential benefits are:

- Modulation of peak demand when there is some degree of coincidence between the PV generation profile and the consumption profile of the building or feeder.
- Thermal relief to distribution equipment, which also implies the possibility of postponing capital investments to increase capacity or replacement.
- Reduction of transmission and distribution losses.
- Voltage support in distribution feeders.
- Reactive power compensation on the feeder.

In relation to the safety and quality aspects of the energy produced, the electricity service supply companies require manufacturers and users of this equipment to comply with article 690 of NOM 001 SEDE 2012 and applicable provisions that guarantee that the installation and operation of the inverter, as well as the photovoltaic system as a whole, is safe and does not adversely affect the quality of the energy.

Theoretical Framework

Climate change is the greatest environmental challenge facing humanity.

The 2015 Paris Agreement was decisive for action, with 195 countries agreeing to limit the global temperature increase of planet Earth to 2 °C by the end of the century compared to the pre-industrial era and to continue efforts to reduce it to 1.5 °C.

Decarbonisation is the process of reducing carbon emissions, especially carbon dioxide (CO_2), into the atmosphere.

The overarching goal is to achieve a low carbon global economy that achieves climate neutrality through the energy transition.

To achieve decarbonisation, it is necessary to decarbonise energy production. By taking advantage of alternative energies it will be possible to supply electricity and mitigate the generation of polluting gases.

At the Universidad Tecnológica de San Juan del Río it is very clear that the use of renewable energies is very profitable to reduce electricity costs and contribute to the care of the environment. Renewable energies have been promoted at the university for several years.

The annual energy consumption is 422.5 MWh, the 79.2 kWp photovoltaic system installed on the roof of the 'K' building provides 30 percent of the energy demanded by the loads installed in the university's teaching and laboratory buildings, and produces an economic saving of 20 percent on the electricity bill paid monthly to the Federal Electricity Commission (Comisión Federal de Electricidad).

The photovoltaic plant interconnected to the grid at the Universidad Tecnológica de San Juan del Río is a clear example of how it is possible to gradually move towards the use of renewable energies, which strengthens the renewable energy career currently offered and places our university in the select group of higher education institutions that implement concrete actions for the care of the environment.

Research question

In higher education institutions in the state of Querétaro, does the cogeneration of electrical energy by means of a photovoltaic system interconnected to the grid allow for the saving of electrical energy, contribute to a reduction in the payment of the electricity bill, and avoid the emission of tons of CO2 into the atmosphere in comparison with higher education institutions without interconnected photovoltaic systems?

Overall objective

To dimension and install a photovoltaic system interconnected to the grid, using the rooftop area of building 'K', which produces 30% of the electrical energy consumed by the electrical equipment installed in the Technological University of San Juan del Río, and which also generates an estimated saving of 20% in the payment of the current bill, based on the current regulations.

Specific objectives

1. To dimension a photovoltaic system interconnected to the grid, which produces 30% of the energy consumed by the electrical equipment installed in the teaching buildings and laboratories of the Universidad Tecnológica de San Juan del Río.

2. To install the photovoltaic panels on the roof of building 'k'.

3. Install the photovoltaic inverters

4. Interconnect the energy produced to the main low voltage board of the 225 kVA, 13.2 kV- 220 V/127 V transformer.

5. Evaluate the energy production using the on-line monitoring system of the photovoltaic system.

Hypothesis

Electrical energy will be generated with a photovoltaic system interconnected to the national electrical system with resources coming from the federation, considering the local solar radiation levels with the objective of being able to increase the operative capacity represented by the electrical energy consumption registered during the year 2017.

In 30% of the energy consumed in the facilities of the university impacting on the costs of electrical energy maintaining at most a monthly payment equivalent to the records of billable demand of the electrical equipment used in the charging period by the ComisiónFederal de Electrticidad (Federal Commission of Electricity).

Methodology

Evaluation of the installation site

The high insolation values present in most of the territory of our country are the basis for the generation of solar photovoltaic and thermal energy. Some factors such as altitude, slope and orientation of the terrain, as well as the shadows produced by the surrounding topography, influence the radiation received (Sánchez, 2023).

In addition to the above, it must also be taken into account that it also depends on the time of day and the time of year. (Edding, 2023).

Box 1

Table 1

Summary of geographical, climatic and meteorological conditions for the project design and implementation site study.

Geographical data (Vdocumento, 2023)	
Location of the installation site	Vista Hermosa, Municipality of San Juan del Río. Querétaro.
Latitude	20.369°
Longitude	-100.010°
Altitude	1978 metres above sea level
Climate and weather data	
Peak solar hours time (in hours) of a hypothetical constant solar irradiance of 1000 W/m^2 (Widiatmika, 2023)	6.19 kWh/m^2/día
Irradiancia	5.6 kW/m^2
Warmest month average temperature (Vdocument, 2023)	25.6°C
Average temperature of the coldest month	7.45°C
Average annual temperature	19°C (10 m from the surface) (Rodriguez, 2023)
Annual precipitation regime	586 mm

There are three types of solar radiation, diffuse, direct and reflected, global radiation is the sum of all three. At the earth's surface it is at best 1000 W/m2. In sizing calculations of solar photovoltaic systems, it is often appropriate to consider the amount of solar radiation reflected

Marroquín de Jesús Ángel, Castillo-Martínez, Luz Carmen, Soto-Álvarez, Sandra and Olivares-Ramírez, Juan Manuel. [2024]. Grid-interconnected photovoltaic system as an alternative to achieve climate neutrality through the energy transition. Journal of Technological Operations. 8[21]1-12: e5821112.
https://doi.org/10.35429/JTO.2024.8.21.1.12

by the surfaces adjacent to the PV modules.

The position of the sun varies during the day and over the seasons, so the angle at which the sun's rays strike a surface also varies. Energy generation depends on the orientation and inclination of the PV modules.

Development of the calculation

The solar radiation values at the site are obtained from National Aeronautics and Space Administration (NASA) data for latitude and longitude at a specific tilt, the recommended optimum tilt will be the latitude of the site with a tolerance of +/- 5°; at a tilt of 20°, the available annual irradiation is 6.19 HSP, but the roof of building 'K' was used, which has a tilt of 15°, a reduction factor of 2.5° annual average needs to be applied, leaving 6.04 HSP.

The photovoltaic power source used is of the Jinko solar brand, model JKM330PP-72 4BB, polycrystalline type, with a linear performance guarantee of 12 years at 90% and 25 years at 80.7% 0 to +3%. Assuming a nominal power tolerance of 0 %, on a 330 W module the power reduction due to dust is considered to be 5 %, so 330 W x 0.95; the output power of the PV power source is reduced above 25°C or increased below 25°C assuming an ambient temperature of 30°C, the effective cell temperature is 30°C + 25°C = 55°C, 30°C above the standard temperature a 313.5 W polycrystalline module with a coefficient of -0.3% per °C, temperature loss = 30°C x 0.3% x °C = 9% the 313.5 W module would lose 9% per temperature to 313.5 x 0.91 = 285.28 W. The system consists of 240 photovoltaic power sources, placed on the roof of the building 'K'.

Calculation report

Characteristics of the photovoltaic energy source:

Box 2

Table 2

Technical data of the photovoltaic module

Rated power STC	330W
Voltage at maximum peak power Vmp	37.80 V
Current at maximum peak power Imp	8.74 A
Open circuit voltage VOC	46.90 V
Short circuit current Isc	9.14 A
Temperature coefficient for open circuit voltage TCvoc	-0.30 %/°C
Total number of modules:	240 pcs. ; 79,200 W

Photovoltaic power source parameters adjusted for temperature.

For the temperature coefficient of the module, we have that:

$$Vt = Voc + (TC \cdot \Delta Temp \cdot Voc). \qquad (1)$$

Where:
Vt = Output voltage at temperature different from 25°C.
TC = Temperature coefficient $\Delta Temp$ = Temperature differential

$$Vt = 46.90V + (-0.0030/°C \cdot (0-25°C) \cdot 46.9V \quad (2)$$
$$Vt = 46.90V + 3.5175V \quad (3)$$
$$Vt = 50.4175 \sim 50V$$

Minimum temperature recorded at the site = 0°C (Col. Vista Hermosa, Municipality of San Juan del Río, Qro.) Inverter: Brand: Fronius, Series: Symo 15.0-3 208/220, inverter power: 15.000 W. (Fronius, 2023)

Box 3

Table 3

Summary of modules and strings by inverter

Maximum MPPT voltage	850 V; 850 V / 50 V= 17 modules
Number of modules per selected chain	= 16
Number of chains	15,000W/330W = 45.45/16 = 2.84 ~ 3 chains

It was decided to place 3 strings of 16 PV power sources each: Open circuit voltage (Voc) of the string adjusted by temperature = 50 V x 16 = 800V (Vdocument, 2023), short-circuit current of each string: 9.14 Amperes. In the photovoltaic source and output circuits the ampacity or conduction capacity of the conductors must be selected with a value of 1.56 times the short-circuit current of the photovoltaic energy source (NOM-001 SEDE 2012, Art.690-8) (Government, 2023) (Idoc, 2023).

Box 4

Table 4

Calculation of conductors and protections according to the short-circuit current of the photovoltaic module

Calculation of conductors (Isc x 1.56)	(NOM-001-SEDE- 2012, 690-8 (a)(1), (b) (1))
Calculation of protections (Isc x 1.25)	(NOM-001-SEDE- 2012, 690-8 (b) (1))

Journal of Technological Operations
Article

Correction factors for ambient temperature (Idoc, 2023)

In accordance with Table No. 310-15(b)(2)(a) of NOM-001-SEDE 2012, for ambient temperatures above 30°C, the current rating shall be corrected by reducing its value, ambient temperatures different from those shown in the ampacity tables shall be corrected following table 310-15(b)(2)(a) or Table 310-15(b)(2)(b) of NOM-001-SEDE-2012. Conductor calculation (Short circuit current x 1.56) = 14.26 A, in accordance with NOM-001-SEDE-2012, 690-8(a)(1), (b)(1)).

Cable temperature range = 75°C. Maximum ambient temperature: 25.6°C + 22°C = 47.6°C (22°C are added from table 310-15(b)(3)(c) of NOM- 001-SEDE-2012 for conductors exposed to sunlight). (Vdocumento, 2023).

Temperature adjustments for sun-exposed ducts on rooftops

Ducts housing conductors are exposed to direct sunlight on rooftops, the values provided in Table 310-15(b)(3)(c) should be added to the outdoor temperature to determine the corresponding ambient temperature for the application of the correction factors in Tables 310-15(b)(2)(a) or 310-15(b)(2)(b). Correction factor: Ampacity /0.75 (for adjusted ambient temperature of 47.6°C) Table No. 310-15(b)(2)(a) of (NOM-001-SEDE 2012). 14.26A / 0.75 = 19.01 A. A total ampacity to be considered for D.C. conductor calculation.

Adjustment of ampacity by number of conductors in a duct

When the number of current-carrying conductors in a duct exceeds three. Where individual conductors or multicore cables are installed without maintaining their spacing over a continuous length in excess of 0.6 m and are not installed in raceways, the allowable ampacity of each conductor shall be reduced as illustrated in Table 310-15(b)(3)(a).

Each current-carrying conductor in a group of conductors in parallel shall be counted as one current-carrying conductor.

This configuration does not apply since there are a maximum of three current-carrying conductors in the same conduit. Ampacity of conductors adjusted to temperature by a) to d) = 19 A.

Summary for conductor selection

Conductor ampacity = 156% of the maximum circuit current, calculated according to NOM-001-SEDE-2012, article 690-8. Conductor ampacity = 9.14 Amperes x 1.56 = 14.26 Amperes. Conductor ampacity adjusted for temperature = 14.26 Amperes/0.75 = 19.01 Amperes (Table No. 310-15(b)(2)(b) of NOM-001-SEDE 2012); therefore, the number of strings per inverter = 3.

Current conductor ampacity in parallel current amperes of 1 string set = 19.01 Amperes; ~ 19 Amperes. Conductor voltage = Temperature adjusted VT module voltage = 50 VDC Temperature adjusted 16-module string voltage = 800 VDC.

Calculation of conductors and protections for direct current

For the calculation of the PV power supply junction box conductor and protections on the DC side. Length of the string conductor furthest from the junction boxes and fuse boxes = 45 metres.

Box 5

Table 5

Voltage drop and DC power loss calculator

DC POWER	DC Voltage Drop	DC Energy losses
DC Voltage (U): 800 V	wire material : Copper	DC Energy losses : 124.54 W
DC Current (Ib): 19 A	Wire size (mm2) : 6	DC Energy losses (%): 0.82 %
DC POWER (P) : 15200 W	Simple lenght (one run) : 45 m	calculate
calculate	DC Drop voltage : 6.56 V	
	DC Drop voltage (%): 0.82	
	calculate	

Conductor size: 10 AWG (6 mm2) shall be used; the conductors of the three strings to junction boxes and shields on the DC side from 1 to 5 are 10 AWG wire, 10 AWG solar cable in thick-walled metal conduit.

Article

In all branches or strings to the junction box and protections on the direct current side, the conductor size of the circuit from the photovoltaic source to the junction box must be selected to avoid a voltage drop of no more than 1% (Vdocument, 2023), as indicated in ANCE-ESP-02.

The maximum current to be conducted is within the permissible range according to table 310- 15(b)(16) of NOM-001-SEDE-2012 (Bedolla, 2023).

Calculation of conductors of junction boxes and protections in direct current to inverters.

Length of conductors from junction box to inverters 1 to 5 = 15 meters (Vdocumento, 2023).

Box 6

Table 6

Voltage drop and DC power loss calculator

10 AWG wire (6 mm2), 10 AWG solar wire in thick-walled metal conduit . Source: http://photovoltaicsoftware.com/DC_AC_drop _voltage_energy_losses_calculator.php

Selection of the junction boxes at the output of the PV generator

To connect the photovoltaic power sources to the junction boxes, the largest gauge conductor compatible with MC4 type connectors that come from the factory in the photovoltaic power sources was considered; 10 AWG gauge and due to the fact that the selection of conductors between the junction boxes and the inverter yields 10 AWG gauge, fuse holders will be used to protect the positive pole as a means of protection and for the negative

conductor the direct passage of the photovoltaic power sources to the input to the inverters.

The IP 65 metal box or enclosure will be used with 15 single-pole fuse holders with sufficient space to house the positive, negative and earthing conductors, as well as the incoming and outgoing conduits.

Conduits and protections at the direct current input to inverters

A 4-inch x 4-inch square metal conduit is used to house the direct current wiring before entering each inverter without mixing with the alternating current wiring as specified in 310-3(c)(2). The disconnect devices included with each inverter and the fuse holders built into the inverter body itself are used for protection.

Alternating current

Calculation of the cable cross-section between the inverter output and the load centre concentrator. For the calculation of the cable cross-section between the inverter output and the load concentrator, a maximum conductor length from the inverters to the AC load centre of 3 metres is considered.

The total number of conductors in the ducting to the AC load centre or AC inverter output concentration point, upper level in the inverter room (inverter numbers 1 to 3); 3+3+3, a total of 9 current-carrying conductors, consider a factor of 80 % (Table 310-15(b)(3)(a), when selecting the conductor ampacity because the conductors of inverter number 1 do not exceed 0.60 m of travel next to the following two inverters: 50 Amperes/0.8 = 62.5 Amperes, by reference to table 310-15(b)(16), the 4 AWG gauge covers the maximum ampacity to be used; calculation result: 4 AWG gauge (21.2 mm2) covers the setting range for ambient temperature.

Lower level in inverter room (inverter numbers 4 and 5); 3+3, a total of 6 current-carrying conductors, a factor of 80 % is considered (Table 310-15(b)(3)(a), when selecting the ampacity of the conductor: 50 Amperes/0.8 = 62.5 A, from Table 310-15(b) (16), 4 AWG gauge covers the maximum amperage to be used, considering a consumption of less than 100 A, the column corresponding to the temperature of 60°C is used for the calculation. 110-14(c)(1)(a).

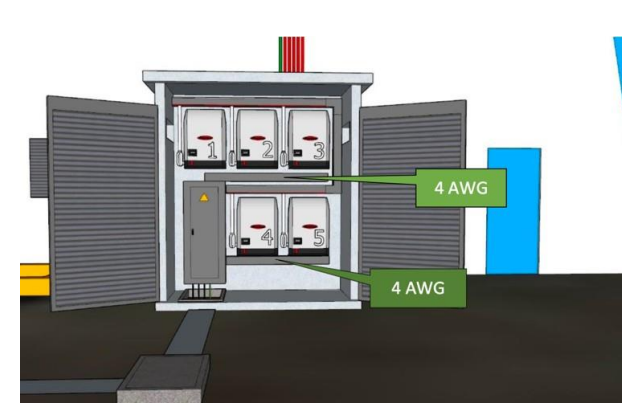Resulting in the calculation: 4 AWG gauge wire (13.3 mm2) (Ecorfan, 2023) .

Box 7

Figure 1

Inverter room

Calculation of cable cross-section from concentrator load centre to output thermal magnetic breaker (TMCB)

It is considered that the length of the conductor from the AC load centre to the output of the main inverter (Bedolla, 2023) TMCB is equal to 1 meter, the maximum ampacity when connecting the five three-phase inverters = 50 Amperes x 5 = 250 Amperes, a maximum current of 250 Amperes will circulate through the bus bars of the connection board, so the board was selected for 400 A, being below the capacity when generating the maximum amperage at maximum irradiation of the PV system. (Vdocument, 2023)

Calculation of the cable cross-section at the output of the inverter and the point of interconnection to the national electricity system, common coupling point.

In the output circuit of the inverter, the conductors must be selected to have a conductive capacity of 1.25 times the current at the rated power of the inverter, the maximum current must be the permanent output current of the inverter 690-8 (a)(3). (Vdocumento, 2023)

Box 8
Table 7

Maximum continuous current output of the inverters

Alternating current voltage	220 Volts
Phases	3; L1, L2, L3, no neutral required for the selected inverter model and configuration.
Maximum continuous current output for each inverter	39. 4 A
Driver ampacity adjusted	39.4 x 1.25=49.25 A ~ 50 A
Number of investors	5

Maximum AC current output of the PV system	250 A

Taking as a reference table 310-15(b)(16) for the type of cable used THHW 90°C, considering consumption greater than 100 A, a column corresponding to a temperature of 75°C is used for the calculation, as indicated in Art. 110-14 (1)(a)(1). The classification according to table 310-15(b)(16) results in the conductor 250 kcmil, applying the temperature correction factor of table 310-15(b)(2)(a) for an ambient temperature of 21-25°C = Amperes x 1.05= 250 A x 1.05 = 262.5 A, so finally the classification of 300 kcmil is selected for this circuit. Review the maximum admissible voltage drop criteria for photovoltaic systems in the AC circuit that does not exceed 2% and considering the distance from the inverter output panel to the switch at the common coupling point = 45 metres.

Selection of the grounding conductor

According to ANCE-ESP-02 'In direct current circuits, the size of the grounding conductor must not be smaller than the size of the conductor with the greatest conduction capacity (thickest wire) as established in Art. 250-93 of NOM 001 SEDE 2012. In no case less than 8.37 mm2 cross section (8 AWG gauge) for copper conductors.

In the case of equipment, the nominal size of copper or aluminium equipment grounding conductors shall not be less than that specified in the following Table (Table 250- 95 of NOM 001 SEDE 2012)'. Since the calculation based on Table 250-122 (NOM-001-SEDE-2012) results in a 14 AWG gauge, the 8 AWG gauge conductor was selected for the entire PV array installed up to the inverter input and from these to the AC concentrator board.

Calculation of protections (Short circuit current Isc x 1.25) 9.14 Amperes x 1.25= 11.43 A (NOM-001-SEDE-2012, 690-8(b) (1)). Direct current protection fuse rating = 15 A, 1000 volts.

From table 250-122 results in 14 AWG gauge and considering that in no case less than 8 AWG gauge; size selected: 8 AWG (16 mm2) green coated copper 7 wires from the PV generator chassis to the paralleling grounding bus at the inverter and from these to the paralleling bus on the AC circuit breaker

concentrator plate.

For the grounding conductor on the AC circuit from the AC circuit breaker panel to the common coupling point (250 A AC) and following the indications in table 250-122, the result is a size smaller than 4 AWG and larger than 6 AWG, therefore: the size selected for the grounding conductor in this arrangement will be 2 AWG from the AC load centre to the common coupling point to have the best possible grounding protection.

Protective devices on the DC side.

PV Generator Switching Point: As DC side protection devices were selected for each of the three strings of each of the 5 PV circuits. In accordance with 690-8 (b)(1) where necessary, overcurrent devices shall be selected as required in (a) through (d) below: a. Conduct not less than 125 percent of the maximum current calculated in 690-8 (a) . Short-circuit current Isc of 9.14 A x 1.25 = 11.43 A. Closest upper commercial fuse = 15 A. String voltage set = 800 volts direct current; fuse to be selected for 1000 volts direct current.

Surge protection in sub-array: Fuse holder with safe disconnection plus integrated disconnector at DC inverter input.

Surge or lightning protection (surge suppressor). As DC surge protection device already included in the Fronius Symo 15.0-3 208/220 inverter.

Protective devices on the AC side

The selected inverter complies with NOM-001-SEDE-2012, article 690-61 and 705-14.

AC disconnection point at the output of the inverters in parallel; for each of the 5 inverters, the 3-pole x 50 A Square DÒ thermomagnetic circuit breaker was selected, and these are contained in a three-phase Square DÒ panel for 400 A and 30 poles. Since this is a three-phase electrical system, load balancing is not necessary.

At the outlet of the load centre which has the individual output circuit breakers for each inverter, a Square DÒ 3 x 250A LAL type thermomagnetic circuit breaker will be placed to lead to another at the point of interconnection to

the local electrical system, an existing I-Line type panel at the outlet of the 300 kVA substation, installed in front of building 'K'.

A Square DÒ Model SDSA50 three-pole, 240 VAC 50 kA, also called secondary lightning arrester, will be connected to the AC main circuit breaker input of the AC voltage concentrator.

In accordance with the CFE-G0100-04 specification, the location of the protections that a photovoltaic generator interconnected to the CFE must have must be described. (Vdocumento, 2023)

Box 9
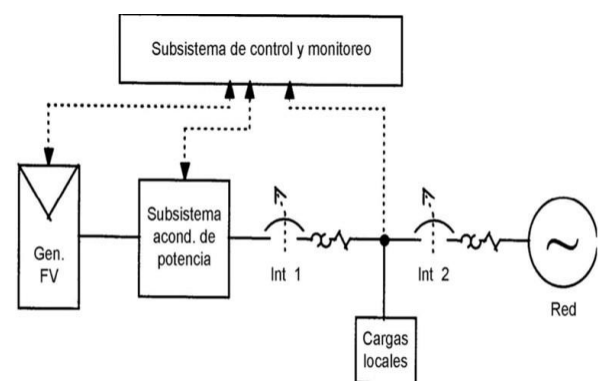
Figure 2

Location of mains disconnect switches, user responsibility

Schematic switch 1; Calculation: Maximum inverter output current x 1.25 x 39.4 A x 1.25 = 49.25 Amps x 4 = 246.25 Amps. Number of phases at the output of the inverter load centre = 3. Selected thermal magnetic circuit breaker = 250 A (Square D, type LAL 3 x 250 Amperes).

Circuit breaker 2 in the diagram refers to the main circuit breaker in the room before the point of common coupling, type I-Line 250 Amps.

Selection of the piping

For the channelling of the DC wiring from the PV source to the inverters, thick-walled metal conduit with the following dimensions was selected: (The conductors in 10 AWG solar cable have a nominal outer sheath diameter of 6.93 mm2, which is their equivalent in THW nominal outer diameter is 8 AWG cable, so this diameter is considered for the conduit calculation).

Photovoltaic output circuit

From the photovoltaic array, strings 1 to 2, there are conductors in positive and negative 10 AWG solar cable plus the 8 AWG earth conductor, giving a total of three conductors (equivalent to 8 AWG); table C-8 of NOM-001-SEDE-2012 gives a diameter of 3/4' (21mm), the following diameter is selected, 1' (27mm) to reduce the effect of temperature due to conduits exposed to sunlight.

From string 2 to string 3, there are two conductors from string 1 plus two conductors from string 2 in a 10 AWG positive and negative solar cable plus the 8 AWG earth ground conductor, a total of five conductors (8 AWG equivalent); from table C-8 results in 1' (27mm) diameter.

From string 3 to the junction box; 3 strings, three positive conductors, three negative conductors plus the grounding wire, a total of 7 conductors 8 AWG in the same conduit. From table C-8 results in a diameter of 1 1/4' (35 mm). The same for the five three-string circuits to the protective enclosure. (Vdocumento, 2023)

Box 10
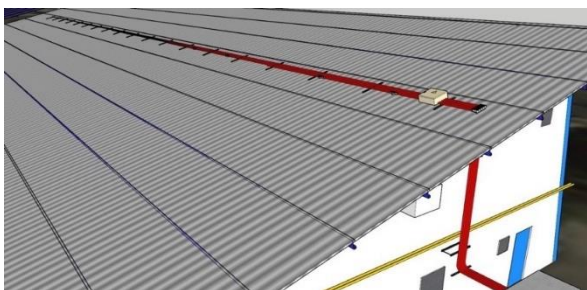
Figure 3

Piping on the roof of the building k

Incoming circuit to inverter

From protection box to collector duct before inverters; 3 strings, positive/negative plus grounding wire, 7 conductors total; 8 AWG (equivalent), for each of the five PV circuits: The same separate conduit layout continues for each PV circuit which has 1 1/4' (35 mm) of metal.

Inside the inverter room a 100 mm x 100 mm square duct is used to receive the conductors of the 5 PV circuits, in total 15 solar positive conductors, 15 solar negative conductors and five grounding conductors in 8 AWG wire,

giving a total of 35 8 AWG (equivalent) conductors, from this duct is sent to each inverter as shown in the following figure.

Box 11
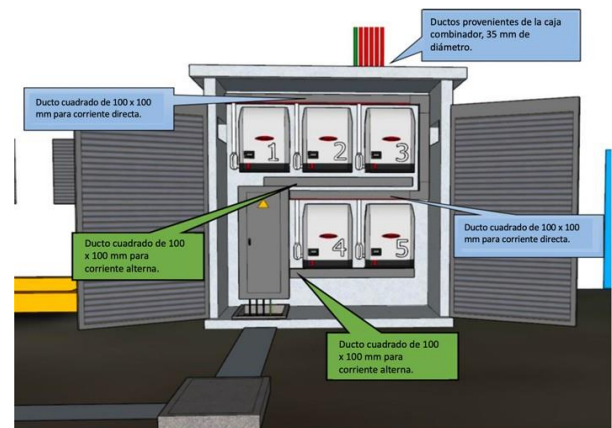
Figure 4

Inverter hut, showing the square duct that houses the DC and AC cables

Inverter output circuit to the AC concentrator panel

From the inverter output to the concentrator panel, a 100 x 100 mm square conduit is used for the 4 AWG AC conductors from inverters 1 to 5. This conduit is independent of the DC circuits.

From the concentrator panel to the interconnection point measuring point

From the concentrator panel to the interconnection point panel, prefabricated and interconnected manholes with 103 mm polyethylene conduit are used to house the three 300 kcmil gauge conductors plus the 2 AWG gauge grounding conductor resulting from the calculation of recommended conductors in table C-8 with a diameter of 2.5' (63mm), a 4' (103mm) conduit will be placed for possible expansion of the photovoltaic system.

Operation of the PV system

The installation of the photovoltaic system was completed in November 2017, at the time of writing this document 354.5 tonnes of CO_2 have been saved from being emitted into the atmosphere, which is equivalent to the amount of CO_2 emitted by a vehicle, travelling a distance of 1,422,557 km, considering that the perimeter of the planet Earth is 40. In economic terms, the savings have been \$1,364,495.43, the system provides 30% of the energy consumed by the equipment installed in the university's

Marroquín de Jesús Ángel, Castillo-Martínez, Luz Carmen, Soto-Álvarez, Sandra and Olivares-Ramírez, Juan Manuel. [2024]. Grid-interconnected photovoltaic system as an alternative to achieve climate neutrality through the energy transition. Journal of Technological Operations. 8[21]1-12: e5821112.
https://doi.org/10.35429/JTO.2024.8.21.1.12

buildings and laboratories; the economic saving is 20% in the payment of the electricity bill paid to the basic services provider.

The photovoltaic system interconnected to the grid has produced a total of 860.45 MWh, in the year 2018 the energy production was 104.34 MWh, this is because the system was interconnected to the grid since March 2018, from 2019 to 2020 the energy production is very similar being approximately 125 MWh, the energy production in the year 2021, decreased by 4.92% compared to 2020. For the years 2022 and 2023 the system produced 131.50, so far in the year 2024, the system has produced 98.84 MWh see figure 5.

Box 12
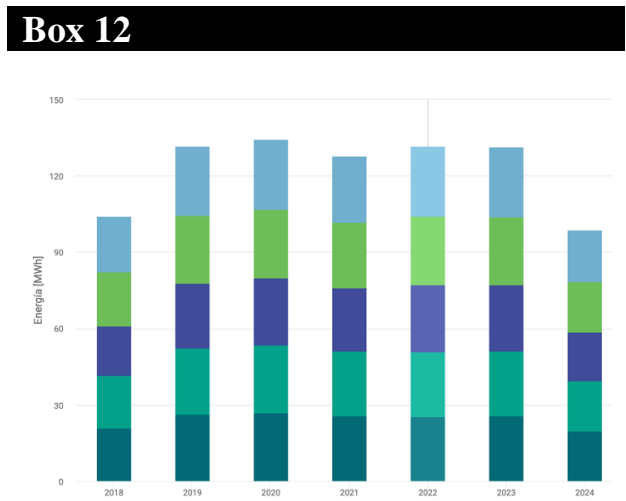
Figure 5

Energy production of the grid-connected PV system

Figure 6 shows the screenshot of the online monitoring system of the electricity production of the 79.2 kWp photovoltaic plant installed on the rooftop of the "K" building of the Technological University of San Juan del Río.. (Vdocumento, 2023)

Box 13
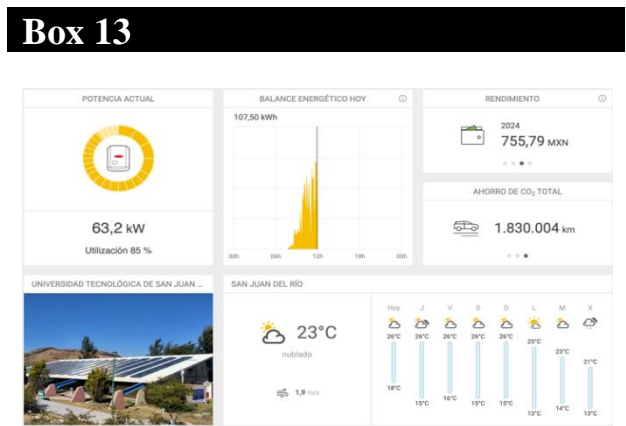
Figure 6

Overview of online monitoring of electricity production for Wednesday 18 September 2024 at 11:56 a.m. CET

Source: https://www.solarweb.com/PvSystems/ PvSystem?pvSystemId=4ba513d4-5bf0- 40c9-beed- 2c46583274ae

The grid-connected photovoltaic system (Sánchez Tello, 2023), places the university in the select group of higher education institutions (Valparaiso, 2023) that produce a percentage of the energy that is consumed, which generates awareness among students, society in general, and takes advantage of renewable energies, which brings environmental benefits.

The Universidad Tecnológica de San Juan del Río is an evaluating and certifying entity (Consejo Nacional de Normalización y Certificación de Competencias Laborales) (CONOCER) and offers training and certification courses in standard EC0586.01 (UTSJR, 2023), entitled installation of photovoltaic systems in residence, commerce and industry. This system has been used as part of the training services currently being offered by the technological services area of the university's department of linkage and complements the training of future engineers in renewable energies at our university.

Box 14

Figure 7

Maintenance activities on the roof of photovoltaic power sources system

Acknowledgements

work, likewise a special thanks to the students of the ES01SM-20 group for the support provided in the maintenance of the photovoltaic system interconnected to the network (Anes, 2023).

Conclusions

The methodology for the design criteria and performance calculation of the PV system is based on what is proposed by the International Renewable Energy Agency (IRENA) (Irena, 2023), which a certified designer must put into practice. The system complies with the regulations in force in our country, to date it has produced 668.87 MWh of energy, which is equivalent to the average consumption of 458 homes of 4 members during a year; it produces 30% of the energy consumed in the laboratories and teaching buildings; there is a saving of 20% in the payment of the bill to the utility company.

According to a quote provided by a company, the maintenance (Rodriguez, 2023) of the 240 photovoltaic power sources costs $2,045.96, and it was suggested to the management that this activity be carried out by students of the renewable energy programme.

The system has been operating without problems; maintenance activities have been carried out on the panels' cover by the students of the ES01SM-20 group, practices that are developed in the renewable energy and photovoltaic systems subjects of the renewable energy engineering curriculum, which contributes to their training.

The use of personal protective equipment for working at heights allows the knowledge acquired (Ortiz, 2023) in the industrial safety subject, which is also part of the renewable energy engineering curriculum, to be put into practice.

The useful life of the equipment is approximately 25 years; it is important to perform maintenance activities on the system, checking all components. This system places the university among the select group of universities that generate a percentage of their energy and contribute to the care of the environment.

References

Alemana, C. (05 de 08 de 2023). energypedia. Obtenido de energypedia.info.

Anes. (17 de 7 de 2023). ANES Obtenido de anes.org.mx.

Aprenderly. (06 de 07 de 2023). APRENDERLY.Obtenido de www.aprenderly.com.

Bedolla, B. C. (01 de 08 de 2023). Ptolomeo. Obtenido de www.ptolomeo.unam.mx.

Cusicahua, W. D. (06 de 08 de 2023). Utc. Obtenido de utc.edu.ec.

Deutsche, C. (03 de 07 de 2023). energypedia. Obtenido de energypedia.info

Electricidad, C. F. (07 de 08 de 2023). scribd. Obtenido de es.scribd.com

Ecorfan. (06 de 08 de 2023). ECORFAN Obtenido de ecorfan.org

Edding, M. E. (07 de 08 de 2023). researchegate. Obtenido de researchegate.net

Energypedia. (23 de 05 de 2022). ENERGYPEDIA. Obtenido de energypedia.info

Fronius. (05 de 08 de 2023). Obtenido de fronius.com.

Gobierno. (16 de 06 de 2023). Gob. Obtenido de Gob.mx.

Harper, E. (15 de 07 de 2023). HARPER.

Harper, E. (15 de 04 de 2023). Harper, E.

Idarrága Velez, A. (06 de 08 de 2023). doku. Obtenido de doku.pub.

Idoc. (04 de 08 de 2023). Idoc .Obtenido de idoc.pub.

Irena. (09 de 08 de 2023). Irena. Obtenido de www.irena.org.

Issuu. (06 de 08 de 2023). ISSUU Obtenido de www.issuu.com.

Lapem. (14 de 06 de 2023). Lapem. Obtenido de Lapem.cfe.gob.mx.

Marroquín, Á. (15 de 02 de 2023). YouTube.

Article

Obtenido de YouTube.com: www.youtube.com

Ortiz, J. G. (01 de 08 de 2023). slideshare. Obtenido de slideshare.net

Patents. (15 de 07 de 2023). PATENTS Obtenido de patents.google.com.

R., G. G. (02 de 08 de 2023). Docplayer. Obtenido de docplayer.es.

Renova-Energía. (07 de 08 de 2023). Renova-Energía. Obtenido de Renova-Energía.com

Rodríguez, M. (08 de 03 de 2023). Addi. Obtenido de Addi.es:

Sánchez Tello, S. (02 de 08 de 2023). repositorio.

Sánchez, C. (03 de 08 de 2023). energynews. Obtenido de energynews.es

Salinas T., E. (02 de 08 de 2023).SALINAS T Doi. Obtenido de doi.org.

Santiago Pérez, D. (06 de 08 de 2023). Santiago Pérez, D. repositorioinstitucional. Obtenido de repositorioinstitucional.buap.mx:

Sarang, A. (04 de 08 de 2023). Sarang, A. idoc. Obtenido de idoc.tips

Solar, J. (13 de 04 de 2023). autosolar. Obtenido de autosolar.es

Tacubarov. (06 de 07 de 2023). Tacubarov Es. Obtenido de es.scribd.com

UTSJR. (27 de 05 de 2023). utsjr. Obtenido de www.utsjr.edu.mx:

Valparaiso, P. U. (06 de 08 de 2023). pucv. Obtenido de www.pucv.cl

Vdocumento. (07 de 08 de 2023). VDOCUMENTOS

Widiatmika, A. (04 de 08 de 2023). Widiatmika, A. idoc. Obtenido de idoc.tips

Instructions for Scientific, Technological and Innovation Publication

[[Title in TNRoman and Bold No. 14 in English and Spanish]

Surname, Name 1st Author*a, Surname, Name 1st Co-authorb, Surname, Name 2nd Co-authorc and Surname, Name 3rd Co-authord [No.12 TNRoman]

a **ROR** [Affiliation institution,](#) **C** [Researcher ID,](#) **iD** [ORC ID,](#) [SNI-CONAHCYT ID](#) or CVU PNPC [No.10 TNRoman]
b **ROR** Affiliation institution, **C** Researcher ID, **iD** ORC ID, SNI-CONAHCYT ID or CVU PNPC [No.10 TNRoman]
c **ROR** Affiliation institution, **C** Researcher ID, **iD** ORC ID, SNI-CONAHCYT ID or CVU PNPC [No.10 TNRoman]
d **ROR** Affiliation institution, **C** Researcher ID, **iD** ORC ID, SNI-CONAHCYT ID or CVU PNPC [No.10 TNRoman]

All ROR-Clarivate-ORCID and CONAHCYT profiles must be hyperlinked to your website.
Prot- **ROR** [University of South Australia](#) • **C** [7038-2013](#)• **iD** [0000-0001-6442-4409](#) • ⊕ 416112

Abstract [In English]
Must contain up to 150 words
Graphical abstract [In English]

Your title goes here		
Objectives	**Methodology**	**Contribution**

Authors must provide an original image that clearly represents the article described in the article. Graphical abstracts should be submitted as a separate file. Please note that, as well as each article must be unique. File type: the file types are MS Office files.No additional text, outline or synopsis should be included. Any text or captions must be part of the image file. Do not use unnecessary white space or a "graphic abstract" header within the image file.

Keywords [In English]
Indicate 3 keywords in TNRoman and Bold No. 10

Abstract [In Spanish]
Must contain up to 150 words
Graphical abstract [In Spanish]

Your title goes here		
Objectives	**Methodology**	**Contribution**

Authors must provide an original image that clearly represents the article described in the article. Graphical abstracts should be submitted as a separate file. Please note that, as well as each article must be unique. File type: the file types are MS Office files.No additional text, outline or synopsis should be included. Any text or captions must be part of the image file. Do not use unnecessary white space or a "graphic abstract" header within the image file.

Keywords [In Spanish]
Indicate 3 keywords in TNRoman and Bold No. 10

RENIECYT
Registro Nacional de Instituciones y Empresas Científicas y Tecnológicas
1702902 CONAHCYT

Instructions for Scientific, Technological and Innovation Publication

Introduction

Text in TNRoman No.12, single space.

General explanation of the subject and explain why it is important.

What is your added value with respect to other techniques?

Clearly focus each of its features.

Clearly explain the problem to be solved and the central hypothesis.

Explanation of sections Article.

Development of headings and subheadings of the article with subsequent numbers

[Title No.12 in TNRoman, single spaced and bold]

Products in development No.12 TNRoman, single spaced.

Including figures and tables-Editable

In the article content any table and figure should be editable formats that can change size, type and number of letter, for the purposes of edition, these must be high quality, not pixelated and should be noticeable even reducing image scale.

[Indicating the title at the bottom with No.10 and Times New Roman Bold]

Box
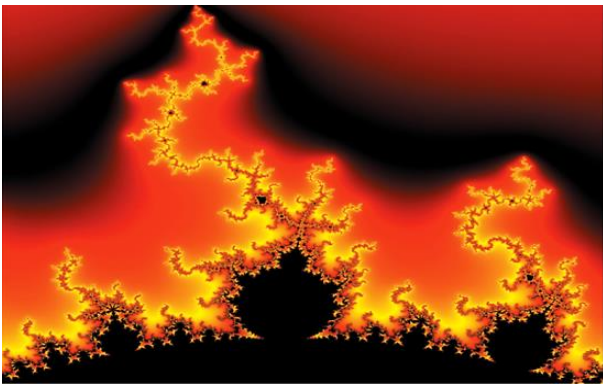
Figure 1

Title [Should not be images-everything must be editable]
Source [in italic]

Box

Table 1

Title [Should not be images-everything must be editable]

Source [in italic]

The maximum number of Boxes is 10 items

For the use of equations, noted as follows:

$$Y_{ij} = \alpha + \sum_{h=1}^{r} \beta_h X_{hij} + u_j + e_{ij} \qquad [1]$$

Must be editable and number aligned on the right side.

Methodology

Develop give the meaning of the variables in linear writing and important is the comparison of the used criteria.

Results

The results shall be by section of the article.

Conclusions

Clearly explain the results and possibilities of improvement.

Annexes

Tables and adequate sources.
The international standard is 7 pages minimum and 14 pages maximum.
Declarations

Conflict of interest

The authors declare no interest conflict. They have no known competing financial interests or personal relationships that could have appeared to influence the article reported in this article.

Surname (IN UPPERCASE), Name 1st Author, Surname (IN UPPERCASE), Name 1st Co-author, Surname (IN UPPERCASE), Name 2nd Co-author and Surname (IN UPPERCASE), Name 3rd Co-author. Paper Title ECORFAN Journal- Taiwan. Year [Times New Roman No. 8]

Instructions for Scientific, Technological and Innovation Publication

Author contribution

Specify the contribution of each researcher in each of the points developed in this research.

Prot-
Benoit-Pauleter, Gerard: Contributed to the project idea, research method and technique.

Availability of data and materials

Indicate the availability of the data obtained in this research.

Funding

Indicate if the research received some financing.

Acknowledgements

Indicate if they were financed by any institution, University or company.

Abbreviations

List abbreviations in alphabetical order.

Prot-
 ANN   Artificial Neural Network

References

Use APA system. Should not be numbered, nor with bullets, however if necessary numbering will be because reference or mention is made somewhere in the Article.

Use the Roman alphabet, all references you have used should be in Roman alphabet, even if you have cited an article, book in any of the official languages of the United Nations [English, French, German, Chinese, Russian, Portuguese, Italian, Spanish, Arabic], you should write the reference in Roman alphabet and not in any of the official languages.

Citations are classified the following categories:

Antecedents. The citation is due to previously published research and orients the citing document within a particular scholarly area.

Basics. The citation is intended to report data sets, methods, concepts and ideas on which the authors of the citing document base their work.

Supports. The citing article reports similar results. It may also refer to similarities in methodology or, in some cases, to the reproduction of results.

Differences. The citing document reports by means of a citation that it has obtained different results to those obtained in the cited document. This may also refer to differences in methodology or differences in sample sizes that affect the results.

Discussions. The citing article cites another study because it is providing a more detailed discussion of the subject matter.

The URL of the resource is activated in the DOI or in the title of the resource.

Prot-
Mandelbrot, B. B. [2020]. Negative dimensions and Hölders, multifractals and their Hölder spectra, and the role of lateral preasymptotics in science. Journal of Fourier Analysis and Applications Special. 409-432.

Intellectual Property Requirements for editing:

- Authentic Signature in Color of Originality Format Author and Coauthors.

- Authentic Signature in Color of the Acceptance Format of Author and Coauthors.

- Authentic Signature in blue color of the Conflict of Interest Format of Author and Co-authors.

Reservation to Editorial Policy

Journal of Technological Operations reserves the right to make editorial changes required to adapt the Articles to the Editorial Policy of the Research Journal. Once the Article is accepted in its final version, the Research Journal will send the author the proofs for review. ECORFAN® will only accept the correction of errata and errors or omissions arising from the editing process of the Research Journal, reserving in full the copyrights and content dissemination. No deletions, substitutions or additions that alter the formation of the Article will be accepted.

Code of Ethics - Good Practices and Declaration of Solution to Editorial Conflicts

Declaration of Originality and unpublished character of the Article, of Authors, on the obtaining of data and interpretation of results, Acknowledgments, Conflict of interests, Assignment of rights and Distribution.

The ECORFAN-Mexico, S.C Management claims to Authors of Articles that its content must be original, unpublished and of Scientific, Technological and Innovation content to be submitted for evaluation.

The Authors signing the Article must be the same that have contributed to its conception, realization and development, as well as obtaining the data, interpreting the results, drafting and reviewing it. The Corresponding Author of the proposed Article will request the form that follows.

Article title:

–   The sending of an Article to Journal of Technological Operations emanates the commitment of the author not to submit it simultaneously to the consideration of other series publications for it must complement the Format of Originality for its Article, unless it is rejected by the Arbitration Committee, it may be withdrawn.

–   None of the data presented in this article has been plagiarized or invented. The original data are clearly distinguished from those already published. And it is known of the test in PLAGSCAN if a level of plagiarism is detected Positive will not proceed to arbitrate.

–   References are cited on which the information contained in the Article is based, as well as theories and data from other previously published Articles.

–   The authors sign the Format of Authorization for their Article to be disseminated by means that ECORFAN-Mexico, S.C. In its Holding Taiwan considers pertinent for disclosure and diffusion of its Article its Rights of Work.

–   Consent has been obtained from those who have contributed unpublished data obtained through verbal or written communication, and such communication and Authorship are adequately identified.

–   The Author and Co-Authors who sign this work have participated in its planning, design and execution, as well as in the interpretation of the results. They also critically reviewed the paper, approved its final version and agreed with its publication.

–   No signature responsible for the work has been omitted and the criteria of Scientific Authorization are satisfied.

–   The results of this Article have been interpreted objectively. Any results contrary to the point of view of those who sign are exposed and discussed in the Article.

Article Title:

Name and Surnames of the Contact Author and the Co-authors	Signature
1.	
2.	
3.	
4.	

Principles of Ethics and Declaration of Solution to Editorial Conflicts

Editor Responsibilities

The Publisher undertakes to guarantee the confidentiality of the evaluation process, it may not disclose to the Arbitrators the identity of the Authors, nor may it reveal the identity of the Arbitrators at any time.

The Editor assumes the responsibility to properly inform the Author of the stage of the editorial process in which the text is sent, as well as the resolutions of Double-Blind Review.

The Editor should evaluate manuscripts and their intellectual content without distinction of race, gender, sexual orientation, religious beliefs, ethnicity, nationality, or the political philosophy of the Authors.

The Editor and his editing team of ECORFAN® Holdings will not disclose any information about Articles submitted to anyone other than the corresponding Author.

The Editor should make fair and impartial decisions and ensure a fair Double-Blind Review.

Responsibilities of the Editorial Board

The description of the peer review processes is made known by the Editorial Board in order that the Authors know what the evaluation criteria are and will always be willing to justify any controversy in the evaluation process. In case of Plagiarism Detection to the Article the Committee notifies the Authors for Violation to the Right of Scientific, Technological and Innovation Authorization.

Responsibilities of the Arbitration Committee

The Arbitrators undertake to notify about any unethical conduct by the Authors and to indicate all the information that may be reason to reject the publication of the Articles. In addition, they must undertake to keep confidential information related to the Articles they evaluate.

Any manuscript received for your arbitration must be treated as confidential, should not be displayed or discussed with other experts, except with the permission of the Editor.

The Arbitrators must be conducted objectively, any personal criticism of the Author is inappropriate.

The Arbitrators must express their points of view with clarity and with valid arguments that contribute to the Scientific, Technological and Innovation of the Author.

The Arbitrators should not evaluate manuscripts in which they have conflicts of interest and have been notified to the Editor before submitting the Article for Double-Blind Review.

Responsibilities of the Authors

Authors must guarantee that their articles are the product of their original work and that the data has been obtained ethically.

Authors must ensure that they have not been previously published or that they are not considered in another serial publication.

Authors must strictly follow the rules for the publication of Defined Articles by the Editorial Board.

The authors have requested that the text in all its forms be an unethical editorial behavior and is unacceptable, consequently, any manuscript that incurs in plagiarism is eliminated and not considered for publication.

Authors should cite publications that have been influential in the nature of the Article submitted to arbitration.

Information services

Indexation - Bases and Repositories

RESEARCH GATE (Germany)
GOOGLE SCHOLAR (Citation indices-Google)
MENDELEY (Bibliographic References Manager)
REDIB (Ibero-American Network of Innovation and Scientific Knowledge- CSIC)
HISPANA (Information and Bibliographic Orientation-Spain)

Publishing Services

Citation and Index Identification H
Management of Originality Format and Authorization
Testing Article with PLAGSCAN
Article Evaluation
Certificate of Double-Blind Review
Article Edition
Web layout
Indexing and Repository
ArticleTranslation
Article Publication
Certificate of Article
Service Billing

Editorial Policy and Management

69 Street. YongHe district, ZhongXin. Taipei-Taiwan. Phones: +52 1 55 6159 2296, +52 1 55 1260 0355, +52 1 55 6034 9181; Email: contact@ecorfan.org www.ecorfan.org

Journal of Technological Operations